Nano Today 47 (2022) 101663

Contents lists available at ScienceDirect

Nano Today

journal homepage: www.elsevier.com/locate/nanotoday

Cycloacceleration of ferroptosis and calcicoptosis for magnetic resonance imaging-guided colorectal cancer therapy

Shuai Guo [a], Zongheng Li [a], Jie Feng [a], Wei Xiong [a], Jing Yang [a], Xuanyi Lu [a], Sugeun Yang [b], Yikai Xu [a], Aiguo Wu [c,*], Zheyu Shen [a,d,**]

[a] Medical Imaging Center, Nanfang Hospital, & School of Biomedical Engineering; Southern Medical University, 1023 Shatai South Road, Guangzhou, Guangdong 510515, China
[b] Department of Biomedical Science, BK21 FOUR Program in Biomedical Science and Engineering, Inha University College of Medicine, Incheon 22212, South Korea
[c] Cixi Institute of Biomedical Engineering, CAS Key Laboratory of Magnetic Materials and Devices, Ningbo Institute of Materials Technology and Engineering, Chinese Academy of Sciences, 1219 Zhongguan West Road, Ningbo, Zhejiang 315201, China
[d] Guangdong Provincial Key Laboratory of Construction and Detection in Tissue Engineering, School of Basic Medical Sciences, Southern Medical University, 1023 Shatai South Road, Guangzhou, Guangdong 510515, China

ARTICLE INFO

Article history:
Received 13 August 2022
Received in revised form 4 October 2022
Accepted 26 October 2022
Available online 2 November 2022

Keywords:
Colorectal cancer (CRC) therapy
Ferroptosis
Calcicoptosis
Cycloacceleration
Magnetic resonance imaging (MRI)

ABSTRACT

Ferroptosis therapy (FT) of the colorectal cancer (CRC) is usually restricted by the relatively slow rate of Fenton reaction due to the limited concentration of intracellular H_2O_2 and the high-level of endogenous H_2S with strong reducibility. To develop an unprecedented strategy for precise targeted CRC theranostics, inspired by the "cyclotron" concept in physics, we propose a new concept of cycloacceleration of ferroptosis and calcicoptosis for the magnetic resonance imaging (MRI)-guided CRC therapy. The developed FGNPs@TA-Fe3/Ca4 nanoparticles have an ideal hydrodynamic diameter of 16.5 ± 2.2 nm and relatively high loading contents of Fe^{3+}/Ca^{2+} (15.6 ± 3.4 % and 32.1 ± 1.9 %). The powerful T_1 imaging ability of FGNPs@TA-Fe3/Ca4 with TME-responsive relaxivities is identified by 7.0 and 3.0 T of MRI scanners. The cycloacceleration of ferroptosis and calcicoptosis induced by FGNPs@TA-Fe3/Ca4 is reinforced by the MTT assay, and the measurements of reactive oxygen species (ROS), lipid peroxide (LPO), glutathione (GSH) peroxidase 4 (GPX4) bioactivity, GSH, H_2S and SO_2 of CT 26 cells with various treatments with or without ferroptosis or calcicoptosis inhibitors. The *in vivo* effectiveness and safety of FGNPs@TA-Fe3/Ca4 for MRI-guided CRC therapy based on cycloacceleration of ferroptosis and calcicoptosis are demonstrated on the CT 26 tumor-bearing BALB/c mice.

Introduction

Colorectal Cancer (CRC) is the third leading cause of cancer death around the world with the trend of rising incidence among young adults [1–5]. At present, clinical imaging diagnosis of CRC is affected by stool and fluid in the intestinal cavity. To provide solid judgment bases and details for clinical diagnosis of CRC disease progress, the enema is required for patients before imaging examination. However, the enema brings pain to patients, causes the secretion of intestinal glands, and sometimes results in more fluid retention, which affects the imaging quality [6–11]. In addition, the clinical CRC treatments lack effective methods for monitoring the disease progression, and the commonly used clinical treatment methods including chemotherapy, radiotherapy, and surgical resection, still have drawbacks, *e.g.*, serious side-effects and risks of recurrences [6,12,13]. Although immune checkpoint blockade therapy (*e.g.*, PD-1/L1, and CTLA-4 inhibitors) [14–16] have been approved for clinical application, its remarkable therapeutic effect could only be observed in a small fraction of patients [17,18]. Furthermore, the immune-related adverse effects (irAEs) have attracted more and more attention [19–22]. To develop unprecedented strategies for precise targeted CRC theranostics, tumor microenvironment (TME)-responsive nanomedicines emerged [13,23,24].

Ferroptosis therapy (FT) is an iron-dependent programmed cell death driven by reactive oxygen species (ROS) generation as well as lipid peroxide (LPO) accumulation on cancer cells membrane [25–29]. Nanomedicine-based FT shows significant penitential to

* Corresponding author.
** Corresponding author at: Medical Imaging Center, Nanfang Hospital, & School of Biomedical Engineering; Southern Medical University, 1023 Shatai South Road, Guangzhou, Guangdong 510515, China.
E-mail addresses: aiguo@nimte.ac.cn (A. Wu), sz@smu.edu.cn (Z. Shen).

https://doi.org/10.1016/j.nantod.2022.101663
1748-0132/

conquer the above-mentioned obstacles for CRC therapy *via* the involved stratergies of ROS amplying and/or LPO accumulation promotion [30–38]. Recently, a growing number of nanomaterials with functions of ROS generation and glutathione peroxidase 4 (GPX4, the ferroptosis downstream regulator) depletion were reported for FT of tumors [30,33,39–45]. However, the relatively slow rate of Fenton reaction due to the limited concentration of intracellular H_2O_2 and the high-level of endogenous H_2S (with strong reducibility) restricts the FT efficiency of CRC [46]. The commonly used ferroptosis agonists, *e.g.*, Erastin (system X^{c-} inhibitor) [47], Sorafenib (system X^{c-} inhibitor) [48], and RSL3 (GPX4 inhibitor) [49], are small molecular drugs with limited water solubility without tumor targetability.

To establish multifunctional nanoplatforms with more sufficient ferroptosis for tumor therapy, we are seeking more synergistic effects in ROS generation and cell membrane destruction. The calcicoptosis was recently defined as a novel programmed cell death caused by Ca^{2+} over-loading that leads to mitochondrional dysfunction with excess ROS generation. Under oxidative stress, the functions of calcium channels in cells are abnormal with difficulties of Ca^{2+} concentration modulation, which further causes cell membrane mineralization by $Ca_3(PO_4)_2$ precipitation [50]. Moreover, ferroptosis also exhibites with great potential of modulation of mitochondrion membrane poteintial (MMP) as well as disruption of cells membranes [51].

In this study, inspired by the "cyclotron" concept in physics, we propose a new concept of cycloacceleration of ferroptosis and calcicoptosis for the magnetic resonance imaging (MRI)-guided high-efficiency CRC therapy. Typically, our previously reported dotted core-shell Fe_3O_4/Gd_2O_3 hybrid nanoparticles (FGNPs), a superior T_1-weighted MRI contrast agent (CA) with a superhigh r_1 (70.0 mM^{-1} s^{-1}) and low r_2/r_1 (1.98) [52], was used for the chelation between tannic acid (TA) and Fe^{3+}/Ca^{2+} on its surface, forming FGNPs@TA-Fe/Ca (Scheme 1). After intravenous injection, the FGNPs@TA-Fe/Ca accumulates at solid tumors based on enhanced permeability and retention (EPR) effect. Under the acidic conditions of late endosomes, the FGNPs@TA-Fe/Ca can release the Ca^{2+}, Fe^{2+} (with electron transferring from the ortho-phenolic hydroxyl groups to Fe^{3+}) on the surface, and the core FGNPs. The released FGNPs with remarkable relaxivities can be used for the MRI-guided CRC therapy. The released Fe^{2+} reacts with the intracellular H_2O_2 (*i.e.*, Fenton reaction) in CRC cells generating ROS, which induces LPO accumulation. Meanwhile, the Fe^{3+} can be reduced to be Fe^{2+} by the relatively high level of glutathione (GSH) in TME, which inhibits GPX4 activity and accelerates LPO accumulation. The LPO accumulation finally results in ferroptosis of CRC cells. Furthermore, the released Ca^{2+} (*i.e.*, Ca^{2+} overloading) can cause dysfunction of mitochondrion with robust ROS generation and biomineralization of cell membrane due to the Ca^{2+} exocytosis and formation of $Ca_3(PO4)_2$ aggregate, which induces calcicoptosis. The excessive ROS generated from Ca^{2+} overloading on mitochondrion can promote LPO accumulation, which accelerates ferroptosis. The ferroptosis can expedite the mitochondrion dysfunction as proved by the mitochondrion membrane potential (MMP) decreasing and biomineralization of cell membranes by Ca^{2+} exocytosis promoted by LPO disruption on the cells membranes, which accelerate calcicoptosis. Therefore, our FGNPs@TA-Fe/Ca can cycloaccelerate ferroptosis and calcicoptosis for high performance MRI-guided CRC therapy.

Results and discussion

Synthesis and characterization of the FGNPs@TA-Fe/Ca nanoparticles

FGNPs used in this study was prepared according to our previously reported procedures [52]. Fig. 1A shows the TEM image of FGNPs with a average size of 5.5 nm, which is almost the same with the reported size.

TA and Fe^{3+} were then chelated on the surface of FGNPs generating FGNPs@TA-Fe1–3 with various synthesis conditions summarized in Table S1. The size distributions measured by dynamic light scattering (DLS, Fig. S1) show only one narrow peak for each sample. The hydrodynamic diameter (d_h) was measured to be 165.5 ± 7.3, 95.8 ± 8.9, and 10.9 ± 2.1 nm for FGNPs@TA-Fe1–3, respectively (Table S1). Because a higher feeding amount of TA and Fe^{3+} caused aggregation of FGNPs@TA-Fe1 and 2, FGNPs@TA-Fe3 was chosen as the optimized sample. The TEM image of FGNPs@TA-Fe3

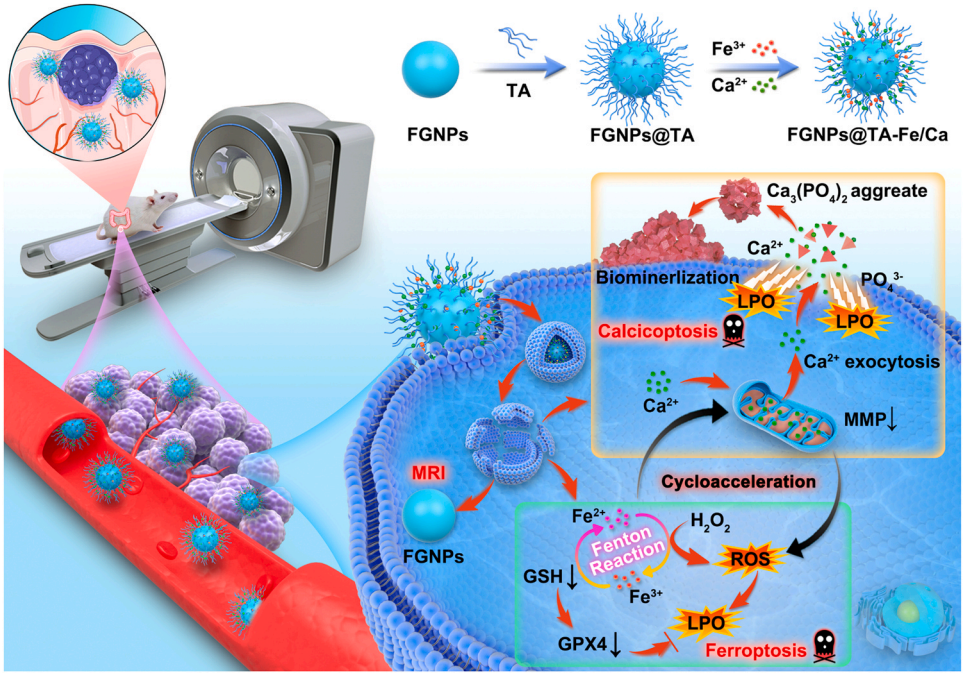

Scheme 1. Schematic illustration for the synthesis of FGNPs@TA-Fe/Ca, and the cycloacceleration principle of ferroptosis and calcicoptosis for MRI-guided tumor therapy based on FGNPs@TA-Fe/Ca.

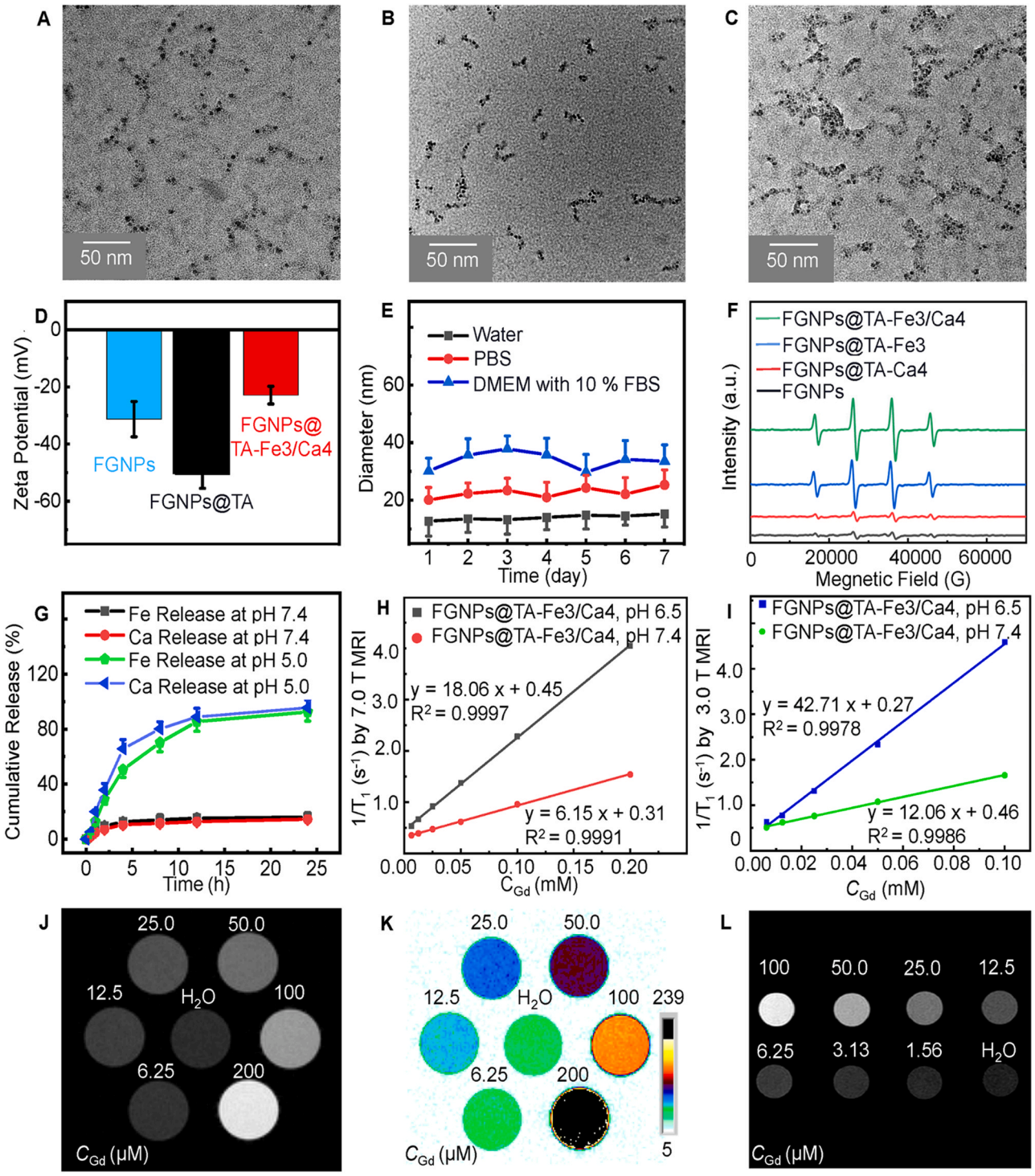

Fig. 1. (A-C): TEM images of FGNPs (A), FGNPs@TA-Fe3 (B) and FGNPs@TA-Fe3/Ca4 (C). (D, E): Zeta potential of FGNPs, FGNPs@TA, and FGNPs@TA-Fe3/Ca4 (D), and stability of FGNPs@TA-Fe3/Ca4 in pure water, PBS, or DMEM with 10 % FBS (E), which were measured by DLS. (F): ESR measurement for FGNPs, FGNPs@TA-Fe3, FGNPs@TA-Ca4, and FGNPs@TA-Fe3/Ca4 incubated at pH 6.5 with H_2O_2 (100 μM) for 6.0 h. (G): Fe and Ca release curves of FGNPs@TA-Fe3/Ca4 at pH 7.4 or 5.0. (H, I): T_1 relaxation rate ($1/T_1$) observed by a 7.0 T (H), or 3.0 T (I) of MRI scanner plotted as a function of C_{Gd} for FGNPs@TA-Fe3/Ca4 (Batch 1) incubated at pH 7.4 or 6.5 for 6.0 h. (J, K): The black & white (J) and corresponding pseudo-color (K) of T_1-weighted MR images for FGNPs@TA-Fe3/Ca4 with various C_{Gd} observed by a 7.0 T MRI scanner (TE = 200.0 ms, TR = 6.3 ms). (L): T_1-weighted MR image of FGNPs@TA-Fe3/Ca4 with various C_{Gd} observed by a 3.0 T clinical MRI system (TE = 400.0 ms, TR = 7.3 ms).

reveals the coating of TA-Fe shell layers by the enhanced contrast in the FGNPs outer sphere (Fig. 1B).

The feeding amount of Ca^{2+} was then optimized to synthesize FGNPs@TA-Fe3/Ca1–4 with various synthesis conditions summarized in Table S2. The d_h measured by DLS (Fig. S2) is respectively 250.5 ± 11.7, 136.5 ± 6.6, and 16.5 ± 2.2 nm for FGNPs@TA-Fe3/Ca2–4 (Table S2). The corresponding data were not shown in for FGNPs@TA-Fe3/Ca1 due to its serious aggregation. Due to the ideal particle size of 16.5 ± 2.2 nm for *in vivo* applications, FGNPs@TA-Fe3/Ca4 was considered to be the optimal sample.

Fig. 1B and C show the TEM images of the optimized sample FGNPs@TA-Fe3 and FGNPs@TA-Fe3/Ca4, respectively. From the TEM

images, it is found that the nanoparticles aggregate slightly because they are observed at dried state without water. The d_h measured by DLS is respectively 10.9 ± 2.1 and 16.5 ± 2.2 nm for FGNPs@TA-Fe3 and FGNPs@TA-Fe3/Ca4, which indicates that the nanoparticles are well-dispersed in water without aggregation. In addition, the loading contents of the Fe and Ca in the FGNPs@TA-Fe3/Ca4 were respectively measured to be 15.6 ± 3.4 % and 32.1 ± 1.9 % by inductively coupled plasma-optical emission spectroscopy (ICP-OES).

The zeta potential of the nanoparticles (Fig. 1D) decreases from − 31.3 ± 6.2 mV (FGNPs) to − 50.7 ± 4.8 mV (FGNPs@TA) indicating the successful coating of negatively charged TA, but then increases to − 22.9 ± 3.1 mV (FGNPs@TA-Fe3/Ca4) demonstrating the significant loading of Fe^{3+} and Ca^{2+}. Moreover, the d_h of the FGNPs@TA-Fe3/Ca4 in water, PBS or DMEM with 10 % FBS measured by DLS has no significant changes in one week (Fig. 1E), which reveals that the FGNPs@TA-Fe3/Ca4 displays good colloidal stability in aqueous solutions.

Fig. S3 shows the structure and Fourier transform infrared (FT-IR) spectra of TA, FGNPs@TA-Fe3/Ca4, and PAA-stabilized FGNPs. The peak *a* at 1510 or 1490 cm^{-1} corresponds to the stretching vibration of benzene -C=C- from TA [53]. The peak *b* at 1435 or 1420 cm^{-1} corresponds to the in-plane bending vibration of $-CH_2-$ from PAA [54]. Both peak *a* and *b* are found in the spectrum of FGNPs@TA-Fe3/Ca4, indicating the successful coating of TA on the surface of PAA-stabilized FGNPs. Fig. S4 shows X-ray Photoelectron Spectroscopy (XPS) spectrum of FGNPs@TA-Fe3/Ca4. The peaks of $Ca2p_{1/2}$ (347.2 eV), $Ca2p_{3/2}$ (352.5 eV) [50], $Fe2p_{1/2}$ (712.2 eV) and $Fe2p_{3/2}$ (717.5 eV) [41] indicate the successful loading of Fe^{3+} and Ca^{2+} on FGNPs@TA-Fe3/Ca4.

To demonstrate the vital role of Fe in cancer FT activated by TME, the ROS generation ability of FGNPs@TA-Fe3/Ca4 was then investigated. The samples of FGNPs, FGNPs@TA-Fe3, FGNPs@TA-Ca4 and FGNPs@TA-Fe3/Ca4 were incubated in PBS with H_2O_2 at pH 6.5 and 37 °C for 6.0 h. With adding of H_2O_2 (with the final concentration of 100 μM) and 5,5-dimeth-yl-1-pyrroline-N-oxide (DMPO) as hydroxyl radical (•OH) trapping agent, the characteristic of •OH peaks appears to be 1:2:2:1 signal (Fig. 1F) [4]. Compared with FGNPs and FGNPs@TA-Ca4, FGNPs@TA-Fe3 and FGNPs@TA-Fe3/Ca4 present higher signal of •OH, which can be attributed to the generated •OH from the Fenton reaction between the released Fe^{2+} and H_2O_2 ($Fe^{2+} + H_2O_2 \rightarrow Fe^{3+} + OH^- + \bullet OH$).

The metal-phenolic networks established by TA chealting with the Gd^{3+}, Fe^{3+} and Ca^{2+} on the surface of FGNPs can be degraded at TME [33]. The corresponding mechanism is illustrated in Scheme S1. The TA-Fe/Ca layer can be degraded due to its pH sensitiviy to release Fe^{2+} (Scheme S1B) [41], Ca^{2+} (Scheme S1C), and FGNPs (Scheme S1D). Fig. 1 G shows the release of Fe^{2+} and Ca^{2+} from the FGNPs@TA-Fe3/Ca4 at pH 5.0 or 7.4 at 37 °C. After incubation for 24 h, the Fe^{2+} and Ca^{2+} release percentages respectively reach 92.5 ± 6.6 % and 95.6 ± 5.7 % at pH 5.0, while only 16.0 ± 3.2 and 14.5 ± 1.66% at pH 7.4. It not only illustrates the responsive release Fe^{2+} and Ca^{2+} from the FGNPs@TA-Fe3/Ca4 in acidic endo/lysosomes, but also demonstrates the stability of the FGNPs@TA-Fe3/Ca4 during the process of blood circulation and the limited side effects at physiological conditions.

T_1 relaxation rate ($1/T_1$) (Fig. 1H and I, and Fig. S5A-D) and T_2 relaxation rate ($1/T_2$) (Fig. S6A-F) observed by a 7.0 T or 3.0 T of MRI scanner are plotted as a function of C_{Gd} for three batches of FGNPs@TA-Fe3/Ca4 incubated at pH 7.4 or 6.5 for 6.0 h. The slopes of linear lines were used as the r_1 or r_2 values [55], and summarized in Table S3. The FGNPs@TA-Fe3/Ca4 (incubated at pH 7.4 for 6.0 h) exhibits a smaller r_1 value (6.17 ± 0.05 mM^{-1} s^{-1} at 7.0 T and 13.18 ± 1.01 mM^{-1} s^{-1} at 3.0 T) and larger r_2/r_1 ratio (11.64 ± 0.42 at 7.0 T and 4.22 ± 0.19 at 3.0 T) due to the bondage of water proton exchange with FGNPs core with a layer of TA-Fe/Ca. However, after incubation of FGNPs@TA-Fe3/Ca4 in pH 6.5 buffer at 37 °C for 6.0 h, the r_1 increases (18.24 ± 0.51 mM^{-1} s^{-1} at 7.0 T and 44.00 ± 2.02 mM^{-1} s^{-1} at 3.0 T) and the r_2/r_1 ratio decreases (9.28 ± 0.21 at 7.0 T and 2.84 ± 0.12 at 3.0 T) significantly, which indicates that the FGNPs core can escape from the FGNPs@TA-Fe3/Ca4 after the pH-sensitive degradation of TA-Fe/Ca layers at acidic TME and then exhibit remarkable MRI performance.

From the black & white (Fig. 1J) and corresponding pseudo-color (Fig. 1K) T_1-weighted MR images of FGNPs@TA-Fe3/Ca4 observed by a 7.0 T of MRI scanner (TE = 200.0 ms, TR = 6.3 ms) and that observed by a 3.0 T of clinical MRI system (TE = 400.0 ms, TR = 7.3 ms) (Fig. 1L), it is obvious that the intensity of T_1 signal increases with increasing of C_{Gd}.

Additionally, ΔSNR is utilized for the quantitative analysis of signal changes, which is calculated according to Eqs. (1) and (2) [52,55–57].

$$SNR = \frac{SI_{mean}}{SD_{noise}} \tag{1}$$

$$\Delta SNR = \frac{SNR_{post} - SNR_{pre}}{SNR_{pre}} \times 100 \ \% \tag{2}$$

Fig. S7 exhibits the ΔSNR values of T_1-weighted MRI at 7.0 T (Fig. 1J), which reinforce the strong dependence of the T_1 signal on Gd concentration gradient.In addition, the intensities of T_1-weighted MR images (pseudo-color) of CT 26 cells treated with FGNPs@TA-Fe3/Ca4 (C_{Gd} = 0.20 mM) are much stronger than that treated with FGNPs (C_{Gd} = 0.20 mM) at any time of treatment (Fig. S8), which also reveals the powerful T_1 imaging ability of the FGNPs@TA-Fe3/Ca4.

The phantom studies illustrate the importance of the pH-sensitivity design of FGNPs@TA-Fe3/Ca4 in the MRI-guided tumor therapy, which exhibits a bright contrast at the tumor location. Besides, the high r_1, low r_2/r_1 and high ΔSNR suggest the potential to be used as an T_1-weighted MRI contrast agent.

Ferroptosis induced by FGNPs@TA-Fe3/Ca4 nanoparticles

To reveal the essential role of intracellular Fe^{2+} for FT, the cellular uptake of nanoparticles by CT 26 cells and the following Fe^{2+} release in acidic late endosomes were investigated by confocal laser scanning microscopy (CLSM). The CT 26 cells were incubated with RMPI 1640 medium (control) or the medium containing nanoparticles including FGNPs, FGNPs@TA-Fe3, FGNPs@TA-Ca4, or FGNPs@TA-Fe3/Ca4 at 37 °C for 3.0 h. The cell nuclei stained with DAPI are blue, the cell cytoskeletons stained with FITC-actin are green, and intracellular Fe^{2+} stained with FeRhoNox-1 is red (Fig. 2A). In the FGNPs@TA-Fe and FGNPs@TA-Fe3/Ca4 groups, it is obvious that lots of intracellular Fe^{2+} (red dots) were released into the cytoplasm from the nanoparticles. In comparison, very few red dots can be observed in the FGNPs and FGNPs@TA-Ca4 groups. This result illustrates the importance of the TA-Fe or TA-Fe/Ca layer on the surface of FGNPs to enhance the intracellular Fe^{2+} level of CT 26 cells for the FT application.

The endo/lysosome escape capabilities of the nanoparticles were also examined by CLSM. After 3.0 h of incubation with RMPI 1640 medium (control) or the medium containing FGNPs, FGNPs@TA-Fe3, FGNPs@TA-Ca4, or FGNPs@TA-Fe3/Ca4 nanoparticles, the CT 26 cells were incubated with the completed medium for another 2.0 h. The cell nuclei stained with DAPI are blue, the endo/lysosomes stained with Endo/Lyso-Tracker are green, and the intracellular Fe^{2+} stained with FeRhoNox-1 is red (Fig. 2B and Fig. S9). Both FGNPs@TA-Fe3 and FGNPs@TA-Fe3/Ca4 groups display numerous red dots that are not overlapped with the green dots, however, both FGNPs and FGNPs@TA-Ca4 groups do not. This result demonstrates that the endo/lysosome escape abilities can be enhanced by TA-Fe coating on the surface of FGNPs, which is in accordance with previous reports [58].

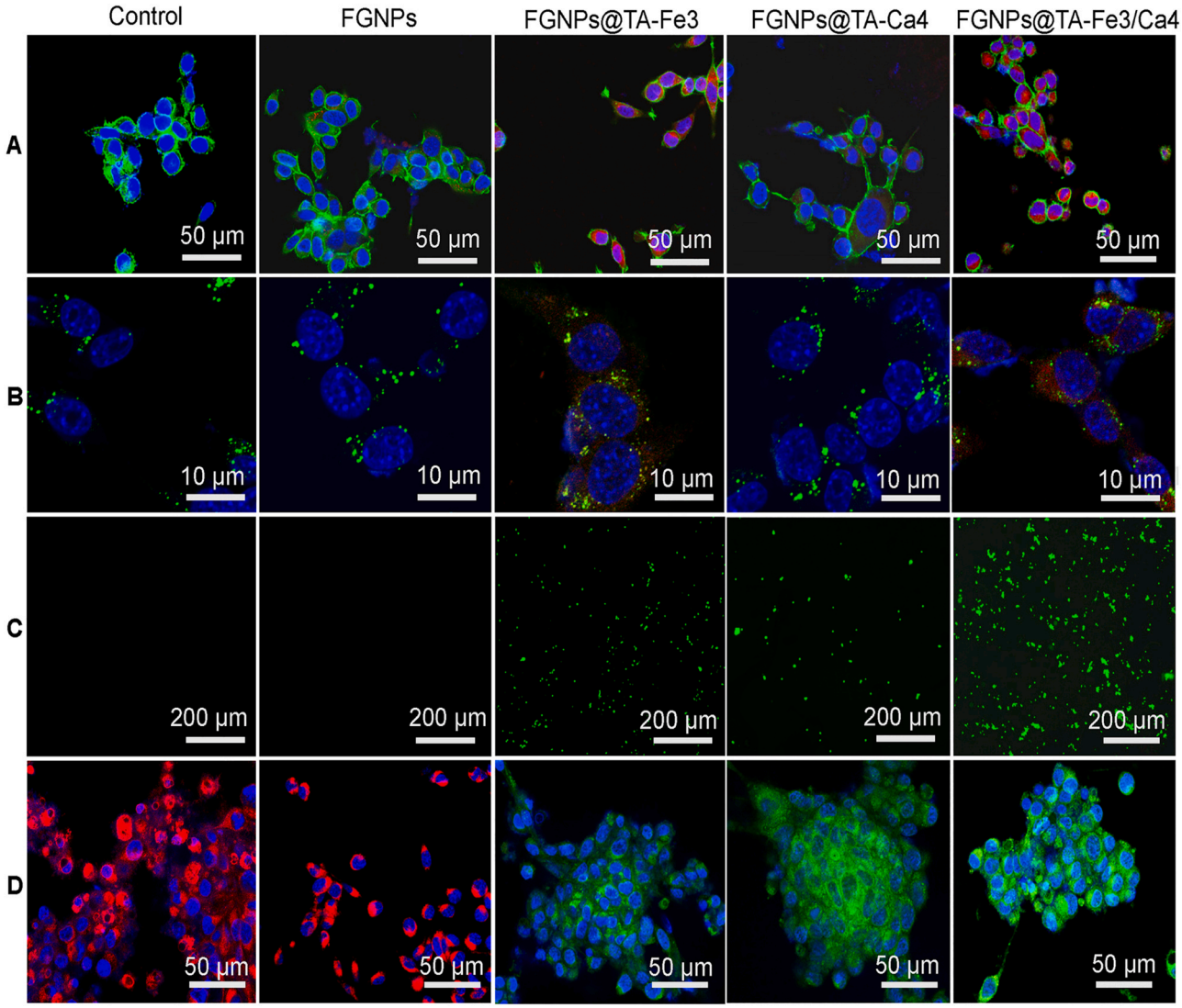

Fig. 2. (A-D): CLSM images of CT 26 cells treated with RMPI 1640 medium (control), or the medium containing nanoparticles (FGNPs, FGNPs@TA-Fe3, FGNPs@TA-Ca4, or FGNPs@TA-Fe3/Ca4). The cells were stained with DAPI (cells nuclei, blue), FITC-actin (cytoskeleton, green) and FeRhoNox-1 (intracellular Fe^{2+}, red) to observe the cellular uptake of Fe (A), stained with DAPI, Endo/Lyso-Tracker (endo/lysosomes, green) and FeRhoNox-1 to observe the endo/lysosome escape of Fe (B), stained with DCFH-DA (green) to indicate the ROS production (C), or stained with DAPI (cells nuclei, blue) and BODIPY C11–581/591 (green/red) to demonstrate the LPO generation (D).

Subsequently, the excessive intracellular ROS generated from Fenton reaction by the high level of intracellular Fe^{2+} and H_2O_2 were also detected by CLSM. The CT 26 cells were stained with a ROS-sensitive fluorescence probe (*i.e.*, 2′,7′-dichlorofluorescein diacetate, DCFH-DA). As shown in Fig. 2C, the FGNPs group exhibits almost no green fluorescence due to the limited intracellular Fe^{2+}. On the contrary, the FGNPs@TA-Fe3 and FGNPs@TA-Ca4 groups show obvious green fluorescence indicating the ROS generation in CT 26 cells, which can be respectively attributed to the accelerated Fenton reaction with ROS generation induced by the released Fe^{2+} and the mitochondrial dysfunction with robust ROS generation resulted from the Ca^{2+} over-loading. Furthermore, the FGNPs@TA-Fe3/Ca4 group presents much stronger green fluorescence suggesting significantly higher ROS level, which demonstrates that the FGNPs@TA-Fe3/Ca4 can cycloaccelerate ferroptosis and calcicoptosis for high performance CRC therapy.

The LPO accumulation was then observed by CLSM using the BODIPY C11–581/591 fluoresce probe (reduced state, red fluorescence; oxidation state, green fluorescence). The process of LPO accumulation could be revealed by the fluorescence transition from red to green. As shown in Fig. 2D, the FGNPs group shows limited LPO accumulation as indicated by the red fluorescence; the FGNPs@TA-Fe3 and FGNPs@TA-Ca4 groups display increased LPO accumulation due to the obvious fluorescence transition from red to green; the FGNPs@TA-Fe3/Ca4 group exhibits very strong green fluorescence without red fluorescence. The strong LPO accumulation in CT 26 cells can be ascribed to the above-mentioned robust ROS generation that oxidize the phospholipid, which is considered the hallmark of ferroptosis [25,59].

To verify the ferroptosis induced by the FGNPs@TA-Fe3/Ca4, more investigations were conducted by utilization of ferroptosis inhibitors, including: 1) the inhibitors that decrease the concentration of intracellular Fe^{2+}/Fe^{3+} to prevent ROS generation from Fenton reaction, *e.g.*, Ferrostatin-1 (Fer-1) [60,61] and deferoxamine (DFO); [48] 2) the inhibitors that activate the GPX4, a central regulator of ferroptosis reducing the toxic LPO to non-toxic hydroxyl lipid (LOH) [42], *e.g.*, GSH (the substrate of GPX4) [59], L-cystine (the substrate of GSH) [62], and N-acetyl-L-cysteine (NAC, a ROS scavenger);[63] 3) the inhibitors with a strong reducibility eliminating oxidizing ROS in cells, *e.g.*, Vitamin C (V_C) [33] and Vitamin E (V_E) [64].

With addition of ferroptosis inhibitors, both ROS and LPO levels in CT 26 cells treated by FGNPs@TA-Fe3/Ca4 were investigated

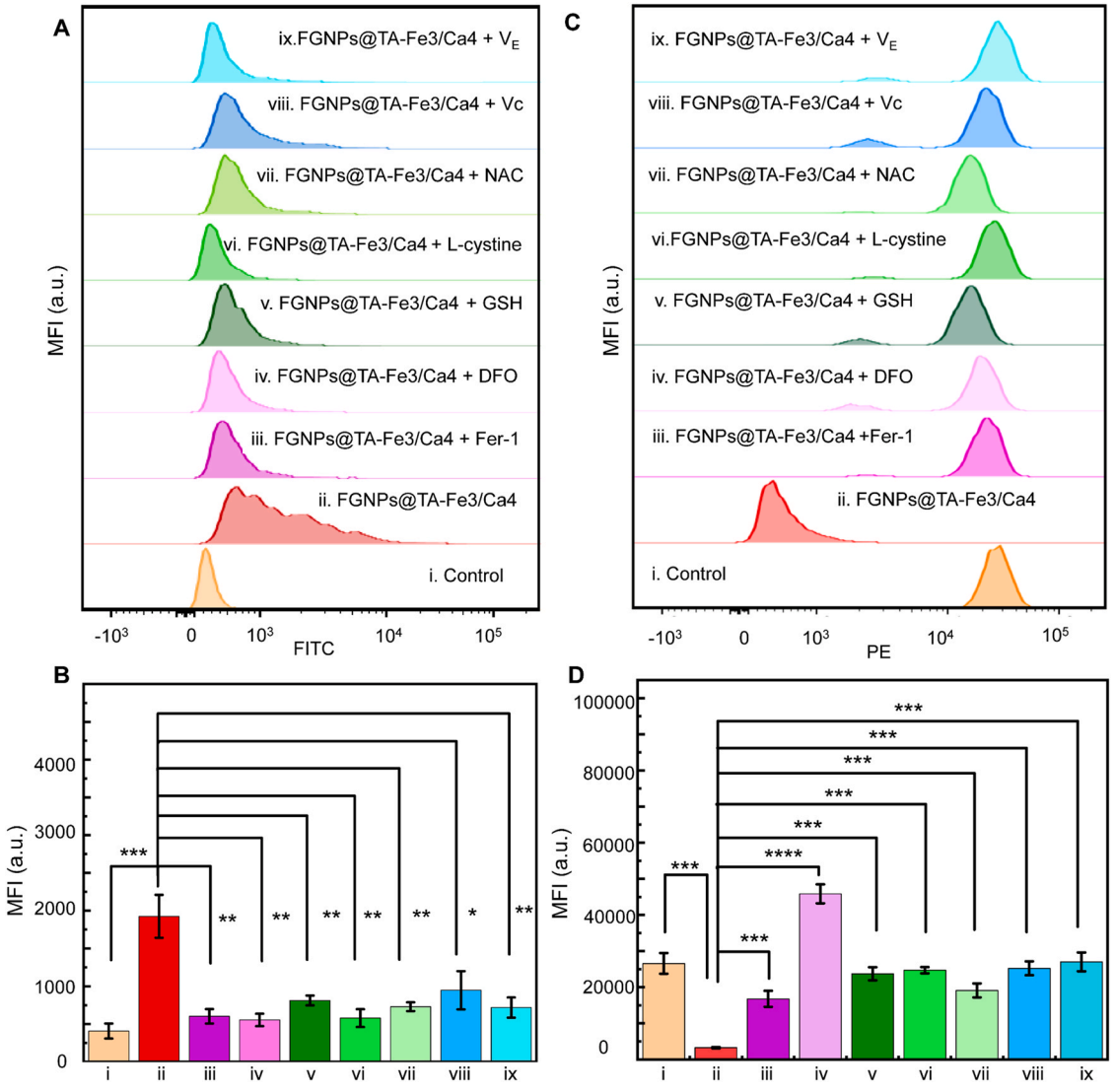

Fig. 3. Fluorescence distribution of the cells treated with FGNPs@TA-Fe3/Ca4 without or with addition of ferroptosis inhibitors including Fer-1 (2.0 μM), DFO (100 μM), GSH (2.0 mM), L-cystine (2.0 mM), NAC (2.0 mM), V_C (25 mM), or V_E (25 mM) measured by flow cytometry (A, C), and the corresponding qualification results (B, D) for the analysis of ROS (A, B) or LPO (C, D) generation, which was stained with DCFH-DA (green), or C11-BODIPY 581/591 (green/red), respectively. Mean ± SD, *P < 0.01, **P < 0.01, ***P < 0.001, ****P < 0.0001.

utilizing flow cytometry. CT 26 cells were incubated with RMPI 1640 medium or the medium containing FGNPs@TA-Fe3/Ca4 for 3.0 h, and then incubated with completed medium with or without ferroptosis inhibitors for another 6.0 h, including Fer-1 (2.0 μM), DFO (100 μM), GSH (2.0 mM), L-cystine (2.0 mM) and NAC (2.0 mM), V_C (25 mM), and V_E (25 mM) [33,65], respectively. Fig. 3A, C show the fluorescence distributions of the cells measured by flow cytometry, Fig. 3B, D present the corresponding qualification results for the analysis of ROS (Fig. 3A, B) or LPO (Fig. 3C, D) generation, which was stained with DCFH-DA (green), or C11-BODIPY 581/591 (green/red), respectively. It can be seen that the FGNPs@TA-Fe3/Ca4 group possesses much stronger green DCFH-DA signal (*i.e.*, higher ROS levels) and much weaker red BODIPY 581/591 signal (*i.e.*, higher LPO levels) than that of the control, and both the ROS and LPO levels decrease significantly with addition of the above-mentioned ferroptosis inhibitors. Therefore, it can be concluded that the FGNPs@TA-Fe3/Ca4 do induce ferroptosis.

Calcicoptosis induced by FGNPs@TA-Fe3/Ca4 nanoparticles

The increasing of intracellular Ca^{2+} level with cellular uptake of FGNPs@TA-Fe3/Ca4 was examined by CLSM. Fig. 4A and Fig. S10 show the CLSM images of CT 26 cells treated with RMPI 1640 medium or the medium containing nanoparticles. The cell nuclei stained with DAPI are blue, and the intracellular Ca^{2+} stained with Fluo-4 AM is green. It is obvious that the control, FGNPs, and FGNPs@TA-Fe3 groups display rare green dots (*i.e.*, intracellular Ca^{2+}). On the contrary, the FGNPs@TA-Ca4 and FGNPs@TA-Fe3/Ca4 groups exhibit numerous green dots, indicating the efficient cellular uptake of FGNPs@TA-Ca4 and FGNPs@TA-Fe3/Ca4, and the following Ca^{2+} release enhancing the intracellular Ca^{2+} level of CT 26 cells.

Then, the endo/lysosome escape of Ca^{2+} was also observed by CLSM. The CT 26 cells were incubated with RMPI 1640 medium (control) or the medium containing nanoparticles. The cells nuclei stained with DAPI are blue, the endo/lysosomes stained with Endo/

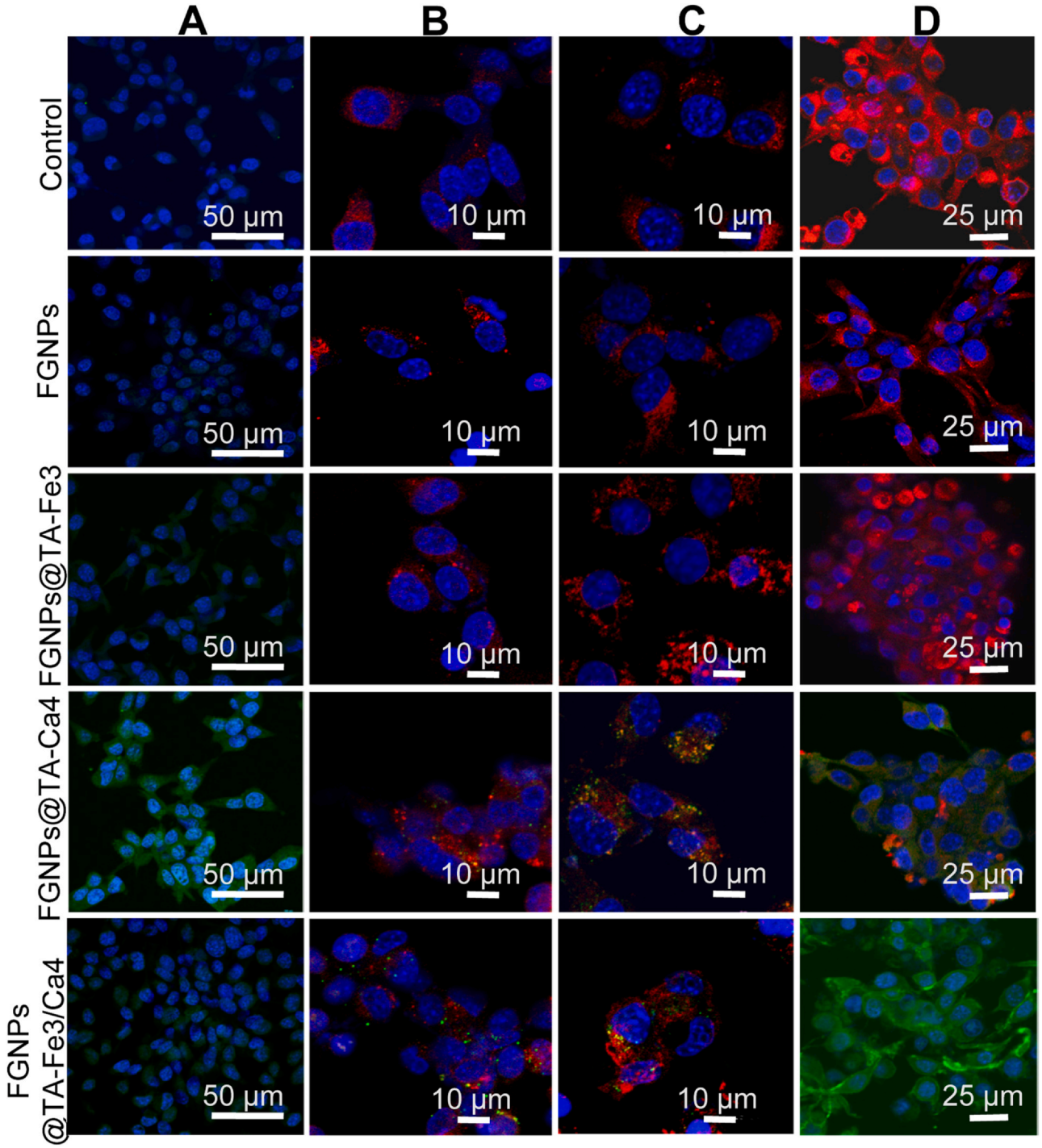

Fig. 4. CLSM images of CT 26 cells incubated with RMPI 1640 medium (control), or the medium containing nanoparticles (FGNPs, FGNPs@TA-Fe3, FGNPs@TA-Ca4, and FGNPs@TA-Fe3/Ca4). The cells were stained with DAPI (cells nuclei, blue) and Fluo-4 AM (intracellular Ca^{2+}, green) to observe the cellular uptake of Ca^{2+} (A), stained with DAPI, Endo/Lyso-Tracker Red (endo/lysosomes, red) and Fluo-4 AM to observe the endo/lysosome escape of Ca^{2+} (B), stained with DAPI, Mito-Tracker Red (mitochondrion, red) and Fluo-4 AM to indicate mitochondrion invasion of Ca^{2+} (C), or stained with stained with of DAPI and JC-1 probe (green/red) to demonstrate MMP decrease caused by Ca^{2+} over-loading (D).

Lyso-Tracker are red, and intracellular Ca^{2+} stained with Fluo-4 AM is green. As shown in Fig. 4B and Fig. S11, rare green dots could be observed in the FGNPs, and FGNPs@TA-Fe3 groups; while the CT 26 cells treated with FGNPs@TA-Ca4 and FGNPs@TA-Fe3/Ca4 display robust green dots out of red dots, which indicates the successful endo/lysosome escape of Ca^{2+}.

Subsequently, the progress of calcicoptosis induced by Ca^{2+} over-loading was also monitored, including: 1) the invasion of intracellular Ca^{2+} into mitochondrion; 2) Ca^{2+} accumulation in the mitochondrion; 3) the MMP decreases and ROS generation induced by mitochondrial Ca^{2+}; 4) biomineralization of the cells membrane caused by Ca^{2+} exocytosis.

The invasion of intracellular Ca^{2+} into mitochondrion was revealed by the CLSM. The cells nuclei stained with DAPI are blue, the mitochondrion stained with Mito-Tracker are red, and intracellular Ca^{2+} stained with Fluo-4 AM is green. As shown in Fig. 4C and Fig. S12, the FGNPs@TA-Ca4 and FGNPs@TA-Fe3/Ca4 groups display over-lapping of the green dots with red dots, suggesting the Ca^{2+} invasion into the mitochondrion.

The mitochondrial Ca^{2+} accumulation was also analyzed by staining of Rod-2 AM (which is a specific mitochondrial Ca^{2+} probe) [50]. The fluorescence distributions (Fig. S13A) and the corresponding quantification results (Fig. S13B) clearly show the increasing amount of mitochondrial Ca^{2+} in FGNPs@TA-Fe3, FGNPs@TA-Ca4 and FGNPs@TA-Fe3/Ca4 groups. It is obvious that the mitochondrial Ca^{2+} accumulation in FGNPs@TA-Ca4 and FGNPs@TA-Fe3/Ca4 groups is caused by the overloading of Ca^{2+}. Surprisingly, the intracellular Ca^{2+} also appears in FGNPs@TA-Fe3 group, which could be attributed to the ROS generated ferroptosis that provoke Ca^{2+} entry of mitochondrion by modulating the Ca^{2+} channels on the plasma membranes [50]. Moreover, the addition of Fer-1 significantly prevents the mitochondrial Ca^{2+} accumulation caused by FGNPs@TA-Fe3/Ca4, which further demonstrate the promotion of ferroptosis to calcicoptosis.

The MMP decrease caused by Ca^{2+} overloading was also tested by the commercial JC-1 (tetrechloro-tetraethyl benzimidazo carbocyanine iodide) probe. It forms aggregates in the normal polarized mitochondrial membrane with red fluorescence, while displays monomers in the damaged and depolarized mitochondrial membrane with green fluorescence [50]. Therefore, the mitochondrial dysfunction could be revealed by fluorescence transition from red to green. As shown in Fig. 4D and Fig. S14, the FGNPs@TA-Ca4 group exhibits obvious green fluorescence transferred from red fluorescence, which reveals the MMP decrease and mitochondrial dysfunction caused by Ca^{2+} overloading. In addition, the FGNPs@TA-Fe3/Ca4 group presents much stronger green fluorescence due to the synergistic effect of mitochondrial Ca^{2+} accumulation, and ferroptosis effect on mitochondrion, including the condensed densities of mitochondrial membrane, the reduction or vanishing of mitochondria crista, and the rupture of outer mitochondrial membranes [66].

In the progress of calcicoptosis, the overloading of Ca^{2+} can induce mitochondrion dysfunction with robust ROS generation. It could be proved by FGNPs@TA-Ca4 treated CT 26 cells, which were chosen as the model to investigate the relationship between ROS generation and mitochondrial Ca^{2+} accumulation. The CT 26 cells were stained by DCFH-DA and Rod2-AM to monitor the dynamic intracellular ROS level increase and mitochondrial Ca^{2+} accumulation by a RT (real-time)-CLSM. As shown in Fig. 5A, the intracellular ROS level is indicated by the green signal and the mitochondrial Ca^{2+} accumulation is revealed by the red signal. The intensity of red and green fluorescence was measured every 80 s. It could be found that both the intracellular ROS level and mitochondrial Ca^{2+} obviously ascend, confirming that Ca^{2+} overloading induces the intracellular ROS level increase in the progress of calcicoptosis. That is because the mitochondrial Ca^{2+} accumulation can stimulate NADPH oxidase activity, followed by ROS production. The ROS level increase can provoke Ca^{2+} entry of mitochondrion by modulating the Ca^{2+} channels and Ca^{2+} ATPases [50].

Biomineralization of the CT 26 cells membranes caused by Ca^{2+} exocytosis was also examined. The CT 26 cells treated by the medium containing FGNPs@TA-Fe3, FGNPs@TA-Ca4 and FGNPs@TA-Fe3/Ca4 were stained by Von Kossa and Alizarin Bordeaux to show the biomineralization of CT 26 cells with black and red dyes. As shown in Fig. 5B. the FGNPs@TA-Fe3/Ca4 treated group is observed with a faster and more frequent accumulation of the black dyes compared with FGNPs@TA-Ca4 treatment at the time point of 12, 15, 18, 24 h. Similarly, as shown in Fig. 5 C, the CT 26 cells treated with FGNPs@TA-Fe3/Ca4 appear with more red dyes than FGNPs@TA-Ca4 at any time points. Moreover, the CT 26 cells treated with FGNPs@TA-Fe3 also exhibits with black dyes (Fig. 5B) and red dyes (Fig. 5 C) at 24 h, which indicates that the ferroptosis plays a role in promoting the progress of biomineralization due to the LPO disruption of the cell's membrane [67], thus leading to intracellular Ca^{2+} releasing and exposing in the extracellular environment, and acceleration of the cell membrane biomineralization.

Cycloacceleration of ferroptosis and calcicoptosis induced by FGNP@TA-Fe3/Ca4

Fig. S15A-C show the cell viabilities of CT 26 cells treated with FGNPs@TA-Fe3, FGNPs@TA-Ca4, or FGNPs@TA-Fe3/Ca4 with or without inhibitors of Fer-1, A23187, DFO, L-cystine, GSH or NAC. The cell viability of CT 26 cells treated with FGNPs@TA-Fe3, FGNPs@TA-Ca4, or FGNPs@TA-Ca4 is 63.4 % (C_{Fe} = 200 μM), 48.7 % (C_{Fe} = 174 μM; C_{Ca}= 55.7 μM), or 20.2 % (C_{Fe} = 200 μM; C_{Ca}= 55.7 μM), respectively. This result indicates that only ferroptosis or calcicoptosis exhibit limited therapeutic efficiency. However, the FGNPs@TA-Fe3/Ca4 show much higher cytotoxicity than that of FGNPs@TA/Fe3 and FGNPs@TA/Ca4 with the same Fe or Ca concentration due to the effect of cycloacceleration of ferroptosis and calcicoptosis. Our FGNPs@TA-Fe/Ca can cycloaccelerate ferroptosis and calcicoptosis because the excessive ROS generated from Ca^{2+} overloading on mitochondrion can promote LPO accumulation accelerating ferroptosis, and the ferroptosis can expedite the mitochondrion dysfunction and biomineralization of cell membrane accelerating calcicoptosis.

To validate the powerfulness of cycloacceleration of ferroptosis and calcicoptosis, the inhibitors of ferroptosis and calcicoptosis were unitized in the MTT assay. With the addition of Fer-1 (2.0 μM), the CT 26 cells treated with FGNPs@TA-Fe3 and FGNPs@TA-Fe3/Ca4 display robust recovery of cell viability (Fig. S15A). The addition of A23187 (8.0 μM), a calcicoptosis inhibitor, also largely enhances the cell viability treated by FGNPs@TA-Ca4 or FGNPs@TA-Fe3/Ca4 (Fig. S15B) because the A23187 can dynamically transport the intracellular Ca^{2+} out of the cells [50]. The inhibitors of L-cystine (2.0 mM), GSH (2.0 mM), and NAC (2.0 mM) significantly increase the viability of cells treated by FGNPs@TA-Fe3/Ca4 (Fig. S15C), suggesting the key role of GPX4 and ROS on ferroptosis. Moreover, with addition of Fer-1 (2.0 μM) and DFO (100 μM), the CT 26 cells treated with FGNPs@TA-Fe3/Ca4 exhibit significantly enhanced viability (Fig. S15A, C), indicating the importance of intracellular Fe^{2+} level on ferroptosis.

Fig. S16 shows CLSM images of CT 26 cells with Live & Dead staining after treatment with RMPI 1640 medium (control), or the medium containing nanoparticles (FGNPs, FGNPs@TA-Fe3, FGNPs@TA-Ca4, and FGNPs@TA-Fe3/Ca4). The FGNPs group displays green dots, illustrating the living cells. Both FGNPs@TA-Fe3 and FGNPs@TA-Ca4 groups exhibit numerous red dots (the dead cells) among green dots. The FGNPs@TA-Fe3/Ca4 group presents majority of dead cells, which is consistent with the above-mentioned MTT results, demonstrating the powerfulness of cycloacceleration of ferroptosis and calcicoptosis.

Fig. 6A-D show the fluorescence distribution of the CT 26 cells after various treatments with staining of DCFH-DA or BODIPY C11–581/591 measured by flow cytometry, and the corresponding qualification results for the analysis of ROS or LPO generation. Fig. 6A (the fluorescence distribution) and Fig. 6B (the corresponding qualification result) indicate the ROS generation situation revealed by green fluorescence. The FGNPs group only exhibits slight increase of MFI, while the FGNPs@TA-Fe3 and FGNPs@TA-Ca4 groups display obvious MFI increase. Meanwhile, the FGNPs@TA-Fe3/Ca4 group presents with significant ($p < 0.001$) increase of MFI compared with the FGNPs@TA-Fe3 and FGNPs@TA-Ca4 groups, which could be attributed to the cycloacceleration of ferroptosis and calcicoptosis in ROS generation. Furthermore, the addition of Fer-1 significantly decreases the ROS generation from FGNPs@TA-Fe3 and FGNPs@TA-Fe3/Ca4 group ($P < 0.0001$). Similarly, the addition of A23187 also significantly decrease the ROS level generated from the FGNPs@TA-Ca4 and FGNPs@TA-Fe3/Ca4 group ($P < 0.001$). The one-side inhibition of ferroptosis or calcicoptosis induced by FGNPs@TA-Fe3/Ca4 leads to the dysfunction of ROS generation, further demonstrating the cycloacceleration of ferroptosis and calcicoptosis in ROS generation.

Fig. 6C (red fluorescence distribution) and Fig. 6D (corresponding quantification analysis) demonstrate the LPO generation level revealed

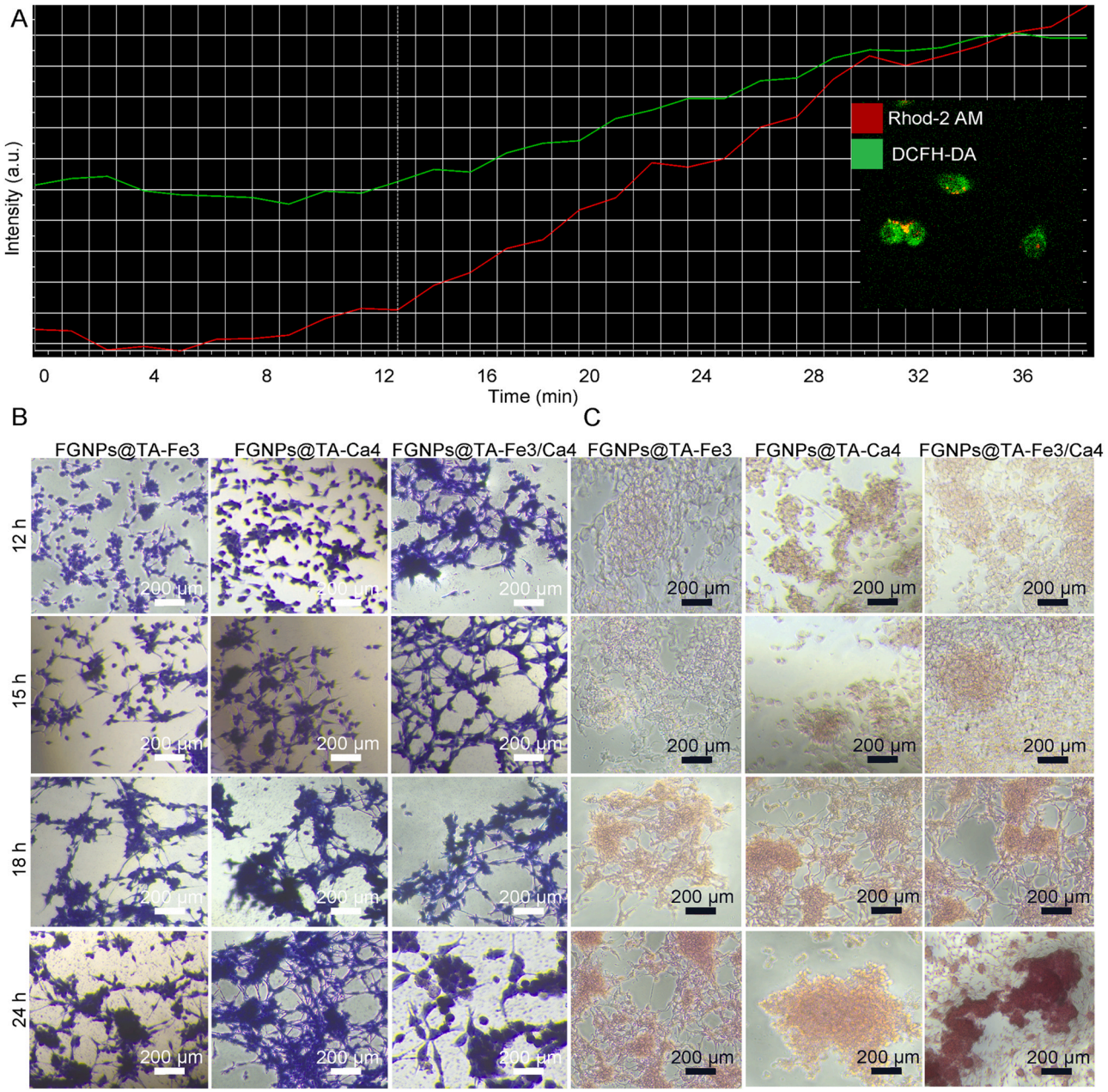

Fig. 5. (A): The fluorescence intensities of intracellular ROS stained with DCFH-DA and mitochondrial Ca^{2+} stained with Rod2-AM from CT 26 cells treated with FGNPs@TA-Ca4, which were monitored by a RT-CLSM. (B, C): Von Kossa (B) and Alizarin Bordeaux (C) staining of the CT 26 cells treated with FGNPs@TA-Fe3, FGNPs@TA-Ca4, or FGNPs@TA-Fe3/Ca4 for various times (12, 15, 18, or 24 h).

by red fluorescence from the oxidative state of BODIPY C11–581/591. The FGNPs group displays with slight decrease of MFI compared with the control group, while the FGNPs@TA-Fe3 and FGNPs@TA-Ca4 exhibit with obvious ($p < 0.01$) decrease of MFI, which could be attributed to the LPO accumulation resulted from the above-mentioned ROS generation. The FGNPs@TA-Fe3/Ca4 group displays more significant ($p < 0.001$) decrease of MFI, illustrating the high LPO accumulation generated from the excessive ROS in the progress of cycloacceleration of ferroptosis and calcicoptosis. With the addition of Fer-1 or A23187, the MFI of FGNPs@TA-Fe3 and FGNPs@TA-Ca4 resume due to the clearance of $Fe^{2+/3+}$ and Ca^{2+} in the cytoplasm by the inhibitors. Interestingly, Fer-1 added to the FGNPs@TA-Fe3/Ca4 group displays significant ($P < 0.01$) MFI recovery, however, the A23187 added to the FGNPs@TA-Fe3/Ca4 group only slightly ($P < 0.05$) elevates the MFI. This result demonstrates that the ferroptosis takes the leading role in the cycloacceleration of ferroptosis and calcicoptosis.

The GPX4 is a central downstream regulator of ferroptosis that can eliminate LPO accumulation. In the progress of cancer FT, the active GPX4 decreases the LPO accumulation. In this study, the GPX4 bioactivity of the treated CT 26 cells was analyzed by the enzyme linked-immune-sorbent assay (ELISA) kits. Fig. 6E shows the qualification of intracellular GPX4 level. The FGNPs group shows no significant changes compared with the control group, while the FGNPs@TA-Fe3 and FGNPs@TA-Ca4 groups exhibit significant ($P < 0.05$) downregulation of the GPX4 bioactivity due to the LPO accumulation. The FGNPs@TA-Fe3/Ca4 group displays the strongest GPX4 activity inhibition due to the cycloacceleration of ferroptosis and calcicoptosis in LPO accumulation and downregulation of the GPX4 bioactivity. The addition of inhibitor Fer-1 in the FGNPs@TA-Fe3 or FGNPs@TA-Fe3/Ca4 group and inhibitor A23187 in the FGNPs@TA-Ca4 or FGNP@TA-Fe3/Ca4 group exhibits obvious ($P < 0.01$) recovery of GPX4 bioactivity. Both addition of Fer-1 and

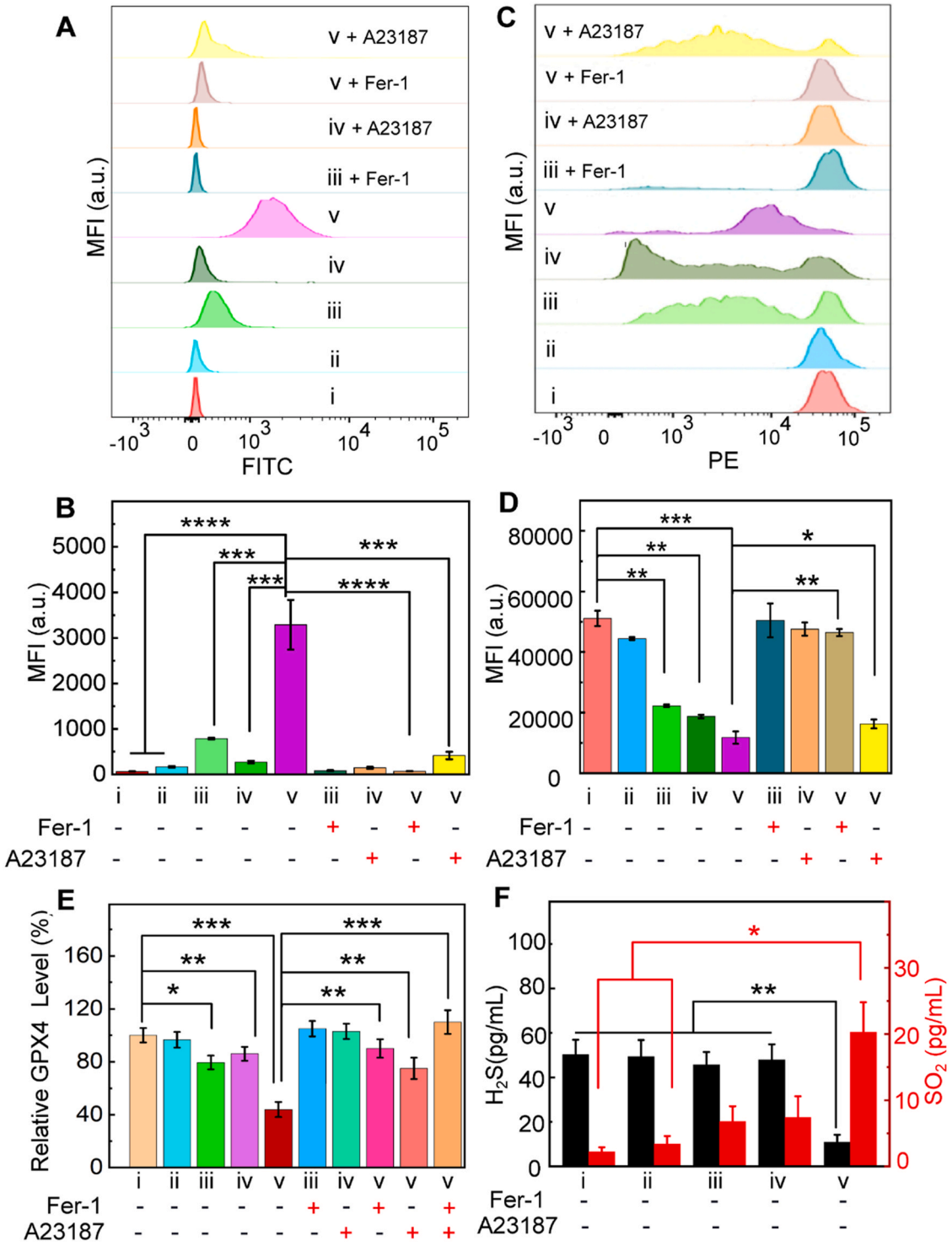

Fig. 6. (A-D): Fluorescence distribution of the CT 26 cells after the treatments of RMPI 1640 medium (i), or the medium containing FGNPs (ii), FGNPs@TA-Fe3 (iii), FGNPs@TA-Ca4 (iv), and FGNPs@TA-Fe3/Ca4 (v) without or with addition of Fer-1 (2.0 μM) or A23187 (8.0 μM) measured by flow cytometry (A, C), and the corresponding qualification results (B, D) for the analysis of ROS (A, B) or LPO (C, D) generation. (E, F): qualification of intracellular GPX4 level (E), H_2S and SO_2 levels (F) of CT 26 cells treated with i-v. Mean ± SD, *P < 0.05, **P < 0.01, ***P < 0.001, ****P < 0.0001.

A23187 in FGNPs@TA-Fe3/Ca4 group presents more significant (P < 0.001) recovery of GPX4 bioactivity.

Similarly, the intracellur GSH levels of CT 26 cells treated with RMPI 1640 medium (control), or the medium containing nanoparticles (FGNPs, FGNPs@TA-Fe3, FGNPs@TA-Ca4, and FGNPs@TA-Fe3/Ca4), with or without A23187 (8.0 M) or Fer-1 (2.0 M) addition are shown in Fig. S17. The change of GSH levels in various groups is similar to that of the GPX4 levels because the GSH is an important substrate of GPX4. Both the GPX4 and GSH assays indicate the effective cooperation of ferroptosis and calcicoptosis.

It is known that the specific physiological feature of CRC is the overexpression of endogenous H_2S caused by the upregulation of cystathionine-β -synthase enzyme [4,46], which inhibits ferroptosis due to its strong reductivity. However, the cycloacceleration of ferroptosis and calcicoptosis induced by our FGNPs@TA-Fe3/Ca4 can decrease the reductivity of the CT 26 cells due to the intracellular

H_2S level descending as tested by ELISA kits. Fig. 6 F shows qualification of intracellular H_2S and SO_2 levels of CT 26 cells with various treatments. It is found that the intracellular H_2S level of CT 26 cells treated with FGNPs@TA-Fe3/Ca4 significantly ($P < 0.001$) decreases, whereas that of FGNPs@TA-Fe3 and FGNPs@TA-Ca4 display with no significant changes of the H_2S level. It could be attributed to the robust intracellular ROS generation from the cycloacceleration of ferroptosis and calcicoptosis induced by FGNPs@TA-Fe3/Ca4. Noticing that the intracellular H_2S are oxidated by ROS, it is proposed that the intracellular H_2S is transferred to SO_2. Thus, the intracellular SO_2 was tested by ELISA kits. As shown in Fig. 6 F, the CT 26 cells with treatment of FGNPs@TA-Fe3/Ca4 exhibit with significant increase of the intracellular SO_2 level accompanied with a decreasing of H_2S level. These results distinctly exhibit the powerfulness of the cycloacceleration of ferroptosis and calcicoptosis in cancer therapy.

In vivo effectiveness and safety evaluations of FGNPs@TA-Fe3/Ca4

Encouraged by the cycloacceleration of ferroptosis and calcicoptosis as examined by CT 26 cells, the pharmacokinetic of FGNPs@TA-Fe3/Ca4 was investigated. By intravenous injection of the FGNPs@TA-Fe3/Ca4 into BALB/c mice, the orbital venous blood was collected at defined time points and then analyzed by ICP-OES. As shown in Fig. 7A, the FGNPs@TA-Fe3/Ca4 shows a half-lifetime ($t_{1/2}$) of 2.42 h in the blood circulation, which indicates that the FGNPs@TA-Fe3/Ca4 is metabolized by the liver, but not the kidney.

It is hypothesized that the FGNPs@TA-Fe3/Ca4 can be accumulated at the tumor location due to the EPR effect [50,68,69]. Based on the pharmacokinetic studies, the biodistribution of the FGNPs@TA-Fe3/Ca4 was also investigated by CT 26 tumor-bearing BALB/c after intravenous injection with the dosage of Fe at 5.0 mg/kg. At the

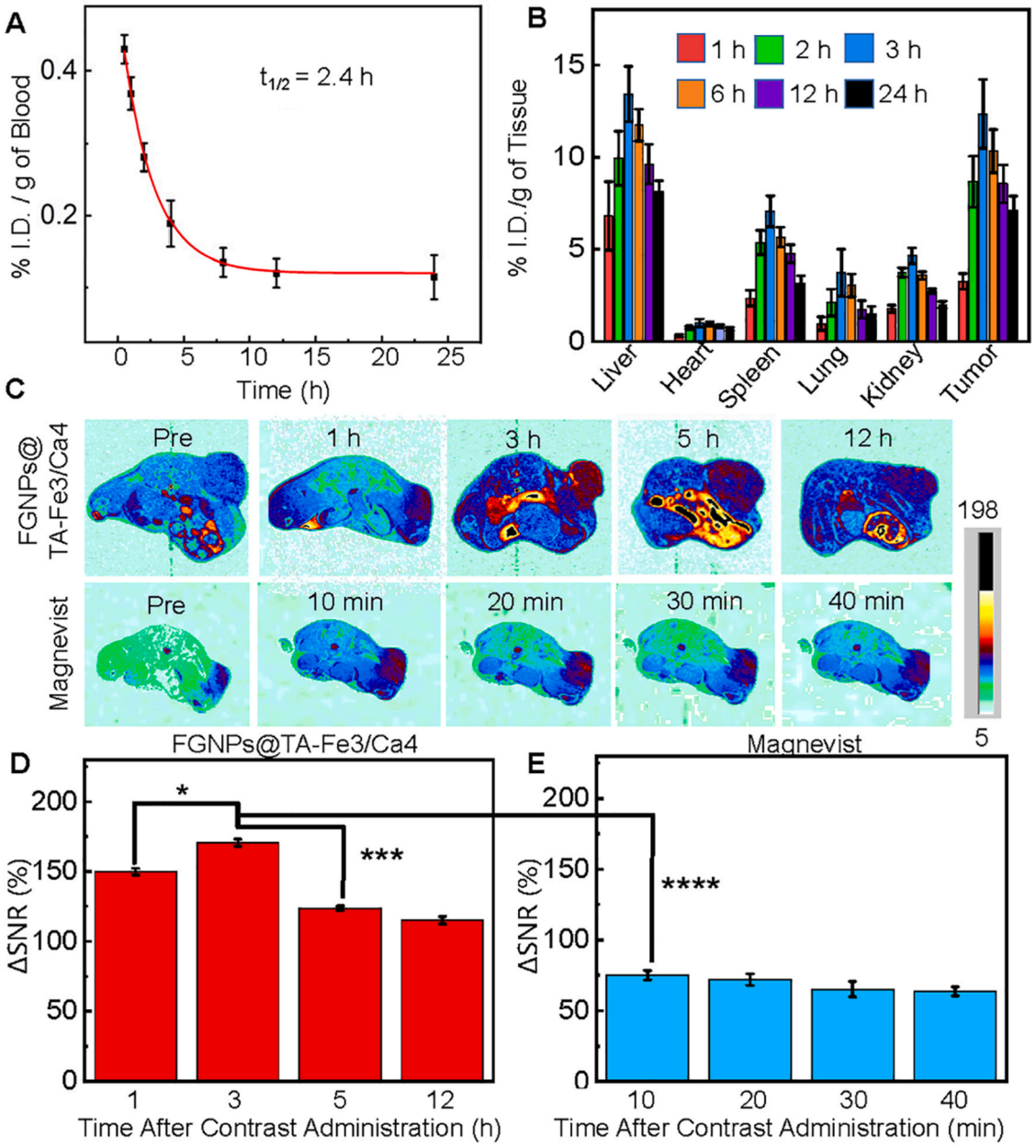

Fig. 7. (A, B): Blood clearance profile (A) and *in vivo* biodistribution (B) of Fe level in the CT 26 tumor-bearing BALB/c mice with intravenous injection of FGNPs@TA-Fe3/Ca4 (Fe dosage: 5.0 mg/kg). (C-E): *In vivo* T_1-weighted MR images (slice orientation: axial; TR = 200.0 ms; TE = 6.3 ms) of CT 26 tumor-bearing BALB/c mice after *i.v.* injection of FGNPs@TA-Fe3/Ca4 (Fe dosage: 5.0 mg/kg) or Magnevist (Gd dosage: 5.0 mg/kg) (C), and the corresponding quantification analysis of the tumor images by ΔSNR (D, E). The MR images before injection are identified as Pre in (C). Mean ± SD, n = 5, * $P < 0.05$, ** $P < 0.01$, * ** $P < 0.001$.

defined time points, the CT 26 tumor-bearing mice were sacrificed for further examination of the Fe concentration in main organs and tumor tissues by ICP-OES, as shown in Fig. 7B. As expected, the tumor uptake of the FGNPs@TA-Fe3/Ca4 at 3.0 h reached 12.34 ± 1.87% I.D./g, and then decreased with the time, which is coincident with the results of pharmacokinetic studies. Moreover, the liver and spleen also display with Fe uptake. Notably, due to the significant difference of intracellular H_2O_2 concentration (20 nM) in somatic cells and tumor cells (50–200 μM) [70], the FGNPs@TA-Fe3/Ca4 can hardly cause side effectsby ferroptosis and calcicoptosis, which could be demonstrated by results of hematoxylin-eosin (H&E) staining (Fig. S18).

Encouraged by the above-mentioned positive results of MRI phantom studies, our FGNPs@TA-Fe3/Ca4 was used for MRI of CT 26 tumors on BALB/c mice compared with the commercial Magnevist. Fig. 7C shows the axial (slice orientation) T_1-weighted MRI of tumor-bearing mice post-injection (*i.v.*) of FGNPs@TA-Fe3/Ca4 or Magnevist. It is obvious that the MRI signal of tumors reaches strongest at 3.0 h post-injection of FGNPs@TA-Fe3/Ca4, which is in accordance with the results of pharmacokinetic. The strongest MRI signal of tumors appears at 20 min post-injection of Magnevist due to its small molecule weight (Mw = 938.0). Besides, the strongest MRI signal of tumors at 3.0 h post-injection of FGNPs@TA-Fe3/Ca4 is much stronger than that at 20 min post-injection of Magnevist. Fig. 7D, E show the corresponding quantification analysis of the tumor images by ΔSNR. The highest tumor ΔSNR is 170.59 ± 2.56% at 3.0 h post-injection of FGNPs@TA-Fe3/Ca4, which is much higher ($P < 0.0001$) than that at 20 min post-injection of Magnevist (75.10 ± 3.30 %). The high MRI efficiency of the FGNPs@TA-Fe3/Ca4 for tumors can be attributed to its high accumulation in the tumors, and the remarkable relaxivities of the FGNPs released in the TME.

The therapeutic efficacy of FGNPs@TA-Fe3/Ca4 was evaluated using CT 26 tumor-bearing BALB/c mice compared with the PBS (control), FGNPs, FGNPs@TA-Fe3, and FGNPs@TA-Ca4 groups (Fig. 8A). The dosage of Fe is 5.0 mg/kg body weight for intravenous injection at day 0. Fig. 8B-D show the relative tumor volume, mice body weight, and survival, respectively. In the PBS and FGNPs groups, the tumors grow exponentially, and one mouse was

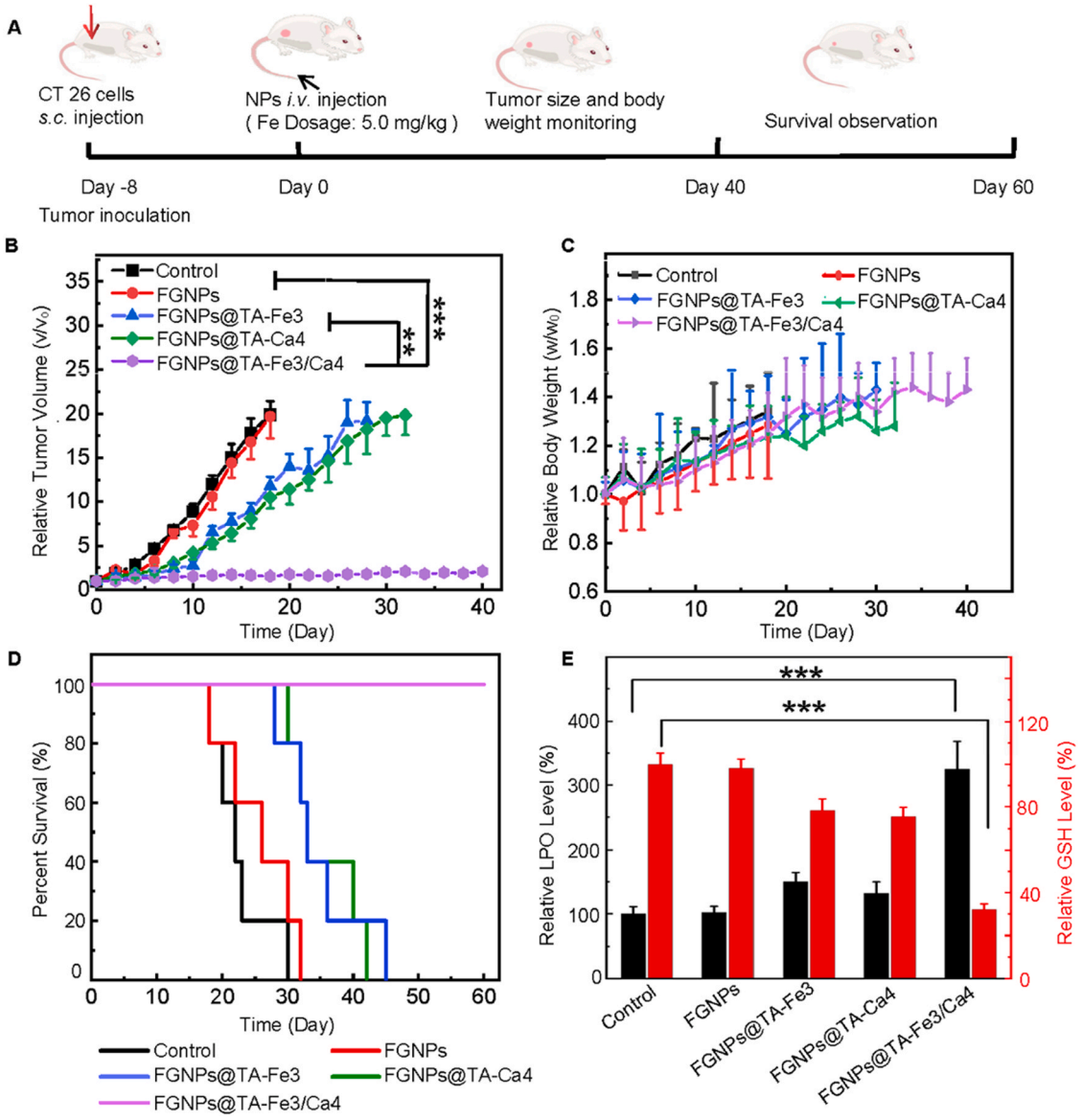

Fig. 8. (A): Schematic illustration of the animal experimental design. (B-D): Tumor growth curves (B), body weight changes (C), and survival (D) of the CT 26 tumor-bearing BALB/c mice after *i.v.* injection of PBS (control), FGNPs, FGNPs@TA-Fe3, FGNPs@TA-Ca4, or FGNPs@TA-Fe3/Ca4 (Fe dosage: 5.0 mg/kg). (E): Relative LPO and GSH level in the treated tumors. Mean ± SD, n = 5, **P < 0.01, ***P < 0.001.

euthanized at day 18 post-injection because of the tumor size over 2000 mm^3. The tumor growth in the groups of FGNPs@TA-Fe3 and FGNPs@TA-Ca4 was initially suppressed, but relapsed over time. However, the tumor growth of the FGNPs@TA-Fe3/Ca4 group was suppressed well, and the mice were all finally survived. The H&E staining of the tumor tissues (Fig. S18) also revealed the extensive CT 26 tumor cells death after treatment with FGNPs@TA-Fe3/Ca4. Fig. 8E shows the relative LPO and GSH level in the treated tumors measured by flow cytometry and ELISA kits. In the FGNPs@TA-Fe3/Ca4 group, the relative LPO concentration shows significant ($P < 0.001$) enhancement than the control groups, and the relative GSH concentration, on the contrary, displays significant ($P < 0.001$) elimination. All these results reinforce the powerfulness of the oxidative stress generated from cycloacceleration of ferroptosis and calcicoptosis.

During the treatment period, the mice in all groups are at a stable growth rate with no significant difference in body weight (Fig. 8C). The H&E assay (Fig. S18) shows the harmlessness of PBS (control), FGNPs, FGNPs@TA-Fe3, FGNPs@TA-Ca4, and the FGNPs@TA-Fe3/Ca4 nanoparticles on the main organs (*i.e.*, heart, liver, spleen, lung, and kidney). More investigations on the toxicity of the FGNPs@TA-Fe3/Ca4 toward a circulatory system and normal tissues were conducted. As shown in Fig. S19, the low hemolysis rate of the FGNPs@TA-Fe3/Ca4 nanoparticles tested by 1.0% red blood corpuscles in PBS illustrates the bio-safety of the FGNPs@TA-Fe3/Ca4.

Conclusions

In summary, inspired by the "cyclotron" concept in physics, we propose a new concept of cycloacceleration of ferroptosis and calcicoptosis for the MRI-guided high-efficiency CRC therapy. Our previously reported FGNPs, a superior T_1-weighted MRI CA with a superhigh r_1 (70.0 mM^{-1} s^{-1}) and low r_2/r_1 (1.98), was used for the chelation between TA and Fe^{3+}/Ca^{2+} on its surface, forming FGNPs@TA-Fe/Ca. The synthesis conditions were optimized and the FGNPs@TA-Fe3/Ca4 was considered to be the optimal sample due to the ideal d_h of 16.5 ± 2.2 nm and the relatively high loading contents of Fe^{3+}/Ca^{2+} (*i.e.*, 15.6 ± 3.4%, and 32.1 ± 1.9%). The successful coating of TA and loading of Fe^{3+}/Ca^{2+} are demonstrated by the measurements of zeta potentials and Fe/Ca release behaviors, and the characterization of TEM, FT-IR, XPS, ESR, and ICP. The powerful T_1 imaging ability of the FGNPs@TA-Fe3/Ca4 with TME-responsive relaxivities is identified by the 7.0 T or 3.0 T of MRI scanner. The mechanism of ferroptosis induced by FGNPs@TA-Fe3/Ca4 nanoparticles is demonstrated by investigations on cells utilizing the ferroptosis inhibitors of Fer-1, DFO, GSH, L-cystine, NAC, V_C, and V_E. The mechanism of calcicoptosis induced by FGNPs@TA-Fe3/Ca4 nanoparticles is indicated by the data on the invasion of intracellular Ca^{2+} into mitochondrion, Ca^{2+} accumulation in the mitochondrion, MMP decrease and ROS generation induced by mitochondrial Ca^{2+}, and biomineralization of the cells membrane caused by Ca^{2+} exocytosis. The cycloacceleration of ferroptosis and calcicoptosis induced by FGNPs@TA-Fe3/Ca4 nanoparticles is reinforced by the MTT assay, and the measurements of ROS, LPO, GPX4 bioactivity, GSH, H_2S and SO_2 of CT 26 cells with various treatments with or without ferroptosis or calcicoptosis inhibitors. The *in vivo* effectiveness and safety of FGNPs@TA-Fe3/Ca4 nanoparticles for MRI-guided colorectal cancer therapy based on cycloacceleration of ferroptosis and calcicoptosis are confirmed on the CT 26 tumor-bearing BALB/c mice. Since We envision that this work shall inspire great interest in designing nanomedicines for ferroptosis and/or calcicoptosis therapy of tumors with more innovations.

Materials and methods

Synthesis of FGNPs@TA-Fe1-3

2.5 mL of FGNPs (C_{Fe} = 2.45 mM; C_{Gd} = 7.56 mM) and 508–127 μL of TA (10 mg/mL) aqueous solutions were added into 17.5 mL of pure water. After stirring for 30 min at room temperature, 400–100 μL of $FeCl_3 0.6 H_2O$ water solution (C_{Fe} = 38.0 μM) aqueous solutions were added into the above FGNPs@TA solutions. After 30 min of reaction under magnetic stirring at room temperature, FGNPs@TA-Fe1–3 (dark blue solutions) were obtained, and then purified by dialysis (Mw cut-off 3000 Da) to remove free Fe^{3+} and TA.

Synthesis of FGNPs@TA-Fe3/Ca1-4

2.5 mL of FGNPs (C_{Fe} = 2.45 mM; C_{Gd} = 7.56 mM) and 127 μL of TA (10 mg/mL) aqueous solutions were added into 17.5 mL of pure water. After stirring for 30 min at room temperature, 100 μL of $FeCl_3 0.6 H_2O$ water solution (C_{Fe} = 38.0 μM) and 800–100 μL of $CaCl_2 0.4 H_2O$ water solution (C_{ca} = 70.0 μM) aqueous solutions were mixed and the mixtures were respectively added into the above FGNPs@TA solution. After further 30 min of reaction under magnetic stirring at room temperature, FGNPs@TA-Fe3/Ca1–4 were obtained, and then purified by dialysis (Mw cut-off 3000 Da) to remove free Ca^{2+}, Fe^{3+} and TA.

Synthesis of FGNPs@TA-Ca4

2.5 mL of FGNPs (C_{Fe} = 2.45 mM; C_{Gd} = 7.56 mM) and 127 μL of TA (10 mg/mL) aqueous solutions were added into 17.5 mL of pure water. After string for 30 min at room temperature, 100 μL of $CaCl_2 0.4 H_2O$ water solution (C_{ca} = 70.0 μM) aqueous solution was added in to the above FGNPs@TA solution. After further 30 min of reaction under magnetic stirring at room temperature, the FGNPs@TA-Ca4 were obtained and then purified by dialysis (Mw cut-off 3000 Da) to remove free Ca^{2+} and TA.

CRediT authorship contribution statement

Shuai Guo: Conceptualization, Methodology, Formal analysis, Investigation, Visualization, Writing – original draft. **Zongheng Li:** Methodology, Formal analysis, Investigation. **Jie Feng:** Resources, Methodology, Investigation. **Wei Xiong:** Resources, Formal analysis, Visualization. **Jing Yang:** Formal analysis, Visualization. **Xuanyi Lu:** Methodology, Visualization. **Sugeun Yang:** Writing – review & editing. **Yikai Xu:** Resources, Writing – review & editing. **Aiguo Wu:** Conceptualization, Resources, Supervision, Writing – review & editing. **Zheyu Shen:** Conceptualization, Methodology, Investigation, Project administration, Resources, Supervision, Writing – review & editing, Funding acquisition.

Data Availability

Data will be made available on request.

Declaration of Competing Interest

The authors declare that they have no known competing financial interests or personal relationships that could have appeared to influence the work reported in this paper.

Acknowledgements

This work was financially supported in part by the Guangdong Provincial Natural Science Foundation of China (2021A1515010605), Guangzhou Key Research and Development Program of China (202103000094), Zhejiang Provincial Natural Science Foundation of China (LR19E030001), and National Natural Science Foundation of China (32271374).

Appendix A. Supporting information

Supplementary data associated with this article can be found in the online version at doi:10.1016/j.nantod.2022.101663.

References

[1] J. Weitz, M. Koch, J. Debus, T. Hohler, P.R. Galle, M.W. Buchler, Colorectal cancer, Lancet 365 (2005) 153-65.
[2] G. Mauri, A. Sartore-Bianchi, A.G. Russo, S. Marsoni, A. Bardelli, S. Siena, Early-onset colorectal cancer in young individuals, Mol. Oncol. 13 (2019) 109–131.
[3] S. Haraldsdottir, H.M. Einarsdottir, A. Smaradottir, A. Gunnlaugsson, T.R. Halfdanarson, Colorectal cancer - review, Laeknabladid 100 (2014) 75–82.
[4] M. Chang, Z. Hou, D. Jin, J. Zhou, M. Wang, M. Wang, M. Shu, B. Ding, C. Li, J. Lin, Colorectal tumor microenvironment-activated bio-decomposable and metabolizable Cu2O@CaCO3nanocomposites for synergistic oncotherapy, Adv. Mater. 32 (2020) 2004647.
[5] Y. Park, Y.M. Ryu, T. Wang, Y. Jung, S. Kim, S. Hwang, J. Park, D.J. Bae, J. Kim, H. Moon, H.S. Lim, S.Y. Kim, E. Chung, K.H. Kim, S. Kim, S.J. Myung, Colorectal cancer diagnosis using enzyme-sensitive ratiometric fluorescence dye and antibody-quantum dot conjugates for multiplexed detection, Adv. Funct. Mater. 28 (2018) 1703450.
[6] L.H. Biller, D. Schrag, Diagnosis and treatment of metastatic colorectal cancer: a review, JAMA 325 (2021) 669–685.
[7] Y. Nasseri, S.J. Langenfeld, Imaging for colorectal cancer, Surg. Clin. North Am. 97 (2017) 503–513.
[8] N.C. Hall, A.T. Ruutiainen, Colorectal cancer:: imaging conundrums, Surg. Oncol. Clin. N. Am. 27 (2018) 289–302.
[9] S. Kijima, T. Sasaki, K. Nagata, K. Utano, A.T. Lefor, H. Sugimoto, Preoperative evaluation of colorectal cancer using CT colonography, MRI, and PET/CT, World J. Gastroenterol. 20 (2014) 16964-75.
[10] P.J. Pickhardt, C. Hassan, S. Halligan, R. Marmo, Colorectal cancer: CT colonography and colonoscopy for detection–systematic review and meta-analysis, Radiology 259 (2011) 393–405.
[11] P.J. Pickhardt, Imaging and screening for colorectal cancer with CT colonography, Radiol. Clin. North Am. 55 (2017) 1183–1196.
[12] E.J. Kuipers, W.M. Grady, D. Lieberman, T. Seufferlein, J.J. Sung, P.G. Boelens, C.J. van de Velde, T. Watanabe, Colorectal cancer, Nat. Rev. Dis. Prim. 1 (2015) 15065.
[13] Y. Li, J. Xin, Y. Sun, T. Han, H. Zhang, F. An, Magnetic resonance imaging-guided and targeted theranostics of colorectal cancer, Cancer Biol. Med. 17 (2020) 307–327.
[14] G. Morad, B.A. Helmink, P. Sharma, J.A. Wargo, Hallmarks of response, resistance, and toxicity to immune checkpoint blockade, Cell 184 (2021) 5309–5337.
[15] D.B. Johnson, C.A. Nebhan, J.J. Moslehi, J.M. Balko, Immune-checkpoint inhibitors: long-term implications of toxicity, Nat. Rev. Clin. Oncol. 19 (2022) 254–267.
[16] X. Guan, F. Polesso, C. Wang, A. Sehrawat, R.M. Hawkins, S.E. Murray, G.V. Thomas, B. Caruso, R.F. Thompson, M.A. Wood, C. Hipfinger, S.A. Hammond, J.N. Graff, Z. Xia, A.E. Moran, Androgen receptor activity in T cells limits checkpoint blockade efficacy, Nature 606 (2022) 791–796.
[17] R.K. Vaddepally, P. Kharel, R. Pandey, R. Garje, A.B. Chandra, Review of indications of FDA-approved immune checkpoint inhibitors per NCCN guidelines with the level of evidence, Cancers 12 (2020) 738.
[18] J.D. Twomey, B. Zhang, Cancer immunotherapy update: FDA-approved checkpoint inhibitors and companion diagnostics, AAPS J. 23 (2021) 39.
[19] S. Shen, H. Dai, Z. Fei, Y. Chai, Y. Hao, Q. Fan, Z. Dong, Y. Zhu, J. Xu, Q. Ma, X. Han, L. Xu, F. Peng, Z. Liu, C. Wang, Immunosuppressive nanoparticles for management of immune-related adverse events in liver, ACS Nano 15 (2021) 9111–9125.
[20] A. Teufel, T. Zhan, N. Härtel, J. Bornschein, M.P. Ebert, N. Schulte, Management of immune related adverse events induced by immune checkpoint inhibition, Cancer Lett. 456 (2019) 80–87.
[21] Z.B. Zengin, N.J. Salgia, A. Chehrazi-Raffle, L. Meza, J. Malhotra, S.K. Pal, Immune related adverse events: classification and management approaches in advanced kidney cancer, Cancer J. 26 (2020) 432–440.
[22] M. Conroy, J. Naidoo, Immune-related adverse events and the balancing act of immunotherapy, Nat. Commun. 13 (2022) 392.
[23] S. Piawah, A.P. Venook, Targeted therapy for colorectal cancer metastases: a review of current methods of molecularly targeted therapy and the use of tumor biomarkers in the treatment of metastatic colorectal cancer, Cancer 125 (2019) 4139–4147.
[24] Y. Ding, Y. Wang, Q. Hu, Recent advances in overcoming barriers to cell-based delivery systems for cancer immunotherapy, Exploration 2 (2022) 20210106.
[25] W.S. Yang, B.R. Stockwell, Ferroptosis: death by lipid peroxidation, Trends Cell Biol. 26 (2016) 165–176.
[26] W. Wang, M. Green, J.E. Choi, M. Gijon, P.D. Kennedy, J.K. Johnson, P. Liao, X. Lang, I. Kryczek, A. Sell, H. Xia, J. Zhou, G. Li, J. Li, W. Li, S. Wei, L. Vatan, H. Zhang, W. Szeliga, W. Gu, R. Liu, T.S. Lawrence, C. Lamb, Y. Tanno, M. Cieslik, E. Stone, G. Georgiou, T.A. Chan, A. Chinnaiyan, W. Zou, CD8+ T cells regulate tumour ferroptosis during cancer immunotherapy, Nature 569 (2019) 270–274.
[27] C. Mao, X. Liu, Y. Zhang, G. Lei, Y. Yan, H. Lee, P. Koppula, S. Wu, L. Zhuang, B. Fang, M.V. Poyurovsky, K. Olszewski, B. Gan, DHODH-mediated ferroptosis defence is a targetable vulnerability in cancer, Nature 593 (2021) 586–590.
[28] L. Jiang, N. Kon, T. Li, S.J. Wang, T. Su, H. Hibshoosh, R. Baer, W. Gu, Ferroptosis as a p53-mediated activity during tumour suppression, Nature 520 (2015) 57–62.
[29] K. Bersuker, J.M. Hendricks, Z. Li, L. Magtanong, B. Ford, P.H. Tang, M.A. Roberts, B. Tong, T.J. Maimone, R. Zoncu, M.C. Bassik, D.K. Nomura, S.J. Dixon, J.A. Olzmann, The CoQ oxidoreductase FSP1 acts parallel to GPX4 to inhibit ferroptosis, Nature 575 (2019) 688–692.
[30] K. Ni, T. Aung, S. Li, N. Fatuzzo, X. Liang, W. Lin, Nanoscale metal-organic framework mediates radical therapy to enhance cancer immunotherapy, Chem 5 (2019) 1892–1913.
[31] X. Chen, C. Yu, R. Kang, G. Kroemer, D. Tang, Cellular degradation systems in ferroptosis, Cell Death Differ. 28 (2021) 1135–1148.
[32] S.J. Dixon, K.M. Lemberg, M.R. Lamprecht, R. Skouta, E.M. Zaitsev, C.E. Gleason, D.N. Patel, A.J. Bauer, A.M. Cantley, W.S. Yang, B. Morrison III, B.R. Stockwell, Ferroptosis: an iron-dependent form of nonapoptotic cell death, Cell 149 (2012) 1060-72.
[33] T. Liu, W. Liu, M. Zhang, W. Yu, F. Gao, C. Li, S.-B. Wang, J. Feng, X.Z. Zhang, Ferrous-supply-regeneration nanoengineering for cancer-cell-specific ferroptosis in combination with imaging-guided photodynamic therapy, ACS Nano 12 (2018) 12181–12192.
[34] Y. Zheng, X. Li, C. Dong, L. Ding, H. Huang, T. Zhang, Y. Chen, R. Wu, Ultrasound-augmented nanocatalytic ferroptosis reverses chemotherapeutic resistance and induces synergistic tumor nanotherapy, Adv. Funct. Mater. 32 (2022) 2107529.
[35] K. Wang, Y. Zhang, W. Mao, W. Feng, S. Lu, J. Wan, X. Song, Y. Chen, B. Peng, Engineering ultrasmall ferroptosis-targeting and reactive oxygen/nitrogen species-scavenging nanozyme for alleviating acute kidney injury, Adv. Funct. Mater. 32 (2022) 2109221.
[36] Y. Du, R. Zhang, J. Yang, S. Liu, J. Zhou, R. Zhao, F. He, Y. Zhang, P. Yang, J. Lin, A "closed-loop" therapeutic strategy based on mutually reinforced ferroptosis and immunotherapy, Adv. Funct. Mater. 32 (2022) 2111784.
[37] S. Yue, P. Zhang, M. Qin, L. Zhu, Y. Qiao, Q. Li, Y. Lu, H. Wu, N. Jiang, C. Liu, M.A. Winnik, Y. Hou, An enzyme-like activity nanoprobe based on Fe(III)–rutin hydrate biomineral for MR imaging and therapy of triple negative breast cancer, Adv. Funct. Mater. 32 (2022) 2202848.
[38] Y. Hao, L. Zhang, Z. Dong, C. Wang, Y. Chao, D. Zhao, Y. Zhu, Z. Yang, N. Yang, Y. Han, L. Feng, Z. Liu, Landscape of myeloid-derived suppressor cell in tumor immunotherapy, Mater. Today 55 (2022) 7.
[39] F. Jiang, B. Ding, S. Liang, Y. Zhao, Z. Cheng, B. Xing, P. Ma, J. Lin, Intelligent MoS2-CuO heterostructures with multiplexed imaging and remarkably enhanced antitumor efficacy via synergetic photothermal therapy/ chemodynamic therapy/ immunotherapy, Biomaterials 268 (2021) 120545.
[40] Z. Li, L. Rong, Cascade reaction-mediated efficient ferroptosis synergizes with immunomodulation for high-performance cancer therapy, Biomater. Sci. 8 (2020) 6272–6285.
[41] T. Ding, Z. Wang, D. Xia, J. Zhu, J. Huang, Y. Xing, S. Wang, Y. Chen, J. Zhang, K. Cai, Long-lasting reactive oxygen species generation by porous redox mediator-potentiated nanoreactor for effective tumor therapy, Adv. Funct. Mater. 31 (2021) 2008573.
[42] Y. Zou, M.J. Palte, A.A. Deik, H. Li, J.K. Eaton, W. Wang, Y.Y. Tseng, R. Deasy, M. Kost-Alimova, V. Dančík, E.S. Leshchiner, V.S. Viswanathan, S. Signoretti, T.K. Choueiri, J.S. Boehm, B.K. Wagner, J.G. Doench, C.B. Clish, P.A. Clemons, S.L. Schreiber, A GPX4-dependent cancer cell state underlies the clear-cell morphology and confers sensitivity to ferroptosis, Nat. Commun. 10 (2019) 1617.
[43] B. Gan, Mitochondrial regulation of ferroptosis, J. Cell Biol. 220 (2021) e202105043.
[44] H. Geng, Q.Z. Zhong, J. Li, Z. Lin, J. Cui, F. Caruso, J. Hao, Metal ion-directed functional metal-phenolic materials, Chem. Rev. 122 (2022) 11432–11473.
[45] Q. Dai, H. Geng, Q. Yu, J. Hao, J. Cui, Polyphenol-based particles for theranostics, Theranostics 9 (2019) 3170–3190.
[46] C. Szabo, C. Coletta, C. Chao, K. Modis, B. Szczesny, A. Papapetropoulos, M.R. Hellmich, Tumor-derived hydrogen sulfide, produced by cystathionine-β-synthase, stimulates bioenergetics, cell proliferation, and angiogenesis in colon cancer, Proc. Natl. Acad. Sci. U.S.A. 110 (2013) 12474-9.
[47] L. Wang, Y. Liu, T. Du, H. Yang, L. Lei, M. Guo, H.F. Ding, J. Zhang, H. Wang, X. Chen, C. Yan, ATF3 promotes erastin-induced ferroptosis by suppressing system Xc, Cell Death Differ. 27 (2020) 662–675.
[48] S. Yuan, C. Wei, G. Liu, L. Zhang, J. Li, L. Li, S. Cai, L. Fang, Sorafenib attenuates liver fibrosis by triggering hepatic stellate cell ferroptosis via HIF-1α/SLC7A11 pathway, Cell Prolif. 55 (2022) e13158.
[49] W.S. Yang, R. SriRamaratnam, M.E. Welsch, K. Shimada, R. Skouta, V.S. Viswanathan, J.H. Cheah, P.A. Clemons, A.F. Shamji, C.B. Clish, L.M. Brown, A.W. Girotti, V.W. Cornish, S.L. Schreiber, B.R. Stockwell, Regulation of ferroptotic cancer cell death by GPX4, Cell 156 (2014) 317–331.
[50] F. Gong, J. Xu, B. Liu, N. Yang, L. Cheng, P. Huang, C. Wang, Q. Chen, C. Ni, Z. Liu, Nanoscale CaH2 materials for synergistic hydrogen-immune cancer therapy, Chem 8 (2022) 268–286.
[51] H. Zhou, X. Lu, C. Du, Z. Zhou, J. Feng, Z. Liang, Y. Xu, X. Qiu, Z. Shen, Cycloacceleration of reactive oxygen species generation based on exceedingly small magnetic iron oxide nanoparticles for tumor ferroptosis therapy, Small 18 (2022) e2202705.

[52] Z. Shen, J. Song, Z. Zhou, B.C. Yung, M.A. Aronova, Y. Li, Y. Dai, W. Fan, Y. Liu, Z. Li, H. Ruan, R.D. Leapman, L. Lin, G. Niu, X. Chen, A. Wu, Dotted core-shell nanoparticles forT1-weighted MRI of tumors, Adv. Mater. 30 (2018) 1803163.
[53] X. Liang, K. Cao, W. Li, X. Li, D.J. McClements, K. Hu, Tannic acid-fortified zein-pectin nanoparticles: Stability, properties, antioxidant activity, and in vitro digestion, Food Res. Int. 145 (2021) 110425.
[54] R. Liu, J. Du, Z. Zhang, H. Li, J. Lu, Y. Cheng, Y. Lv, H. Wang, Preparation of polyacrylic acid-grafted-acryloyl/hemicellulose (PAA-g-AH) hybrid films with high oxygen barrier performance, Carbohydr. Polym. 205 (2019) 83–88.
[55] Z. Shen, T. Chen, X. Ma, W. Ren, Z. Zhou, G. Zhu, A. Zhang, Y. Liu, J. Song, Z. Li, H. Ruan, W. Fan, L. Lin, J. Munasinghe, X. Chen, A. Wu, Multifunctional theranostic nanoparticles based on exceedingly small magnetic iron oxide nanoparticles for T1-weighted magnetic resonance imaging and chemotherapy, ACS Nano 11 (2017) 10992–11004.
[56] Z. Shen, J. Song, B.C. Yung, Z. Zhou, A. Wu, X. Chen, Emerging strategies of cancer therapy based on ferroptosis, Adv. Mater. 30 (2018) 1704007.
[57] Z. Shen, W. Fan, Z. Yang, Y. Liu, V.I. Bregadze, S.K. Mandal, B.C. Yung, L. Lin, T. Liu, W. Tang, L. Shan, Y. Liu, S. Zhu, S. Wang, W. Yang, L.H. Bryant, D.T. Nguyen, A. Wu, X. Chen, Adv. Mater. 15 (2019) 1903422.
[58] J. Chen, J. Li, J. Zhou, Z. Lin, F. Cavalieri, E. Czuba-Wojnilowicz, Y. Hu, A. Glab, Y. Ju, J.J. Richardson, F. Caruso, Metal-phenolic coatings as a platform to trigger endosomal escape of nanoparticles, ACS Nano 13 (2019) 11653–11664.
[59] F. Ursini, M. Maiorino, Lipid peroxidation and ferroptosis: the role of GSH and GPx4, Free Radic. Biol. Med. 152 (2020) 175–185.
[60] P. Liu, Y. Feng, H. Li, X. Chen, G. Wang, S. Xu, Y. Li, L. Zhao, Ferrostatin-1 alleviates lipopolysaccharide-induced acute lung injury via inhibiting ferroptosis, Cell. Mol. Biol. Lett. 25 (2020) 10.
[61] G. Miotto, M. Rossetto, M.L. Di Paolo, L. Orian, R. Venerando, A. Roveri, A.M. Vuckovic, V. Bosello Travain, M. Zaccarin, L. Zennaro, M. Maiorino, S. Toppo, F. Ursini, G. Cozza, Insight into the mechanism of ferroptosis inhibition by ferrostatin-1, Redox Biol. 28 (2020) 101328.
[62] Y. Zhang, R.V. Swanda, L. Nie, X. Liu, C. Wang, H. Lee, G. Lei, C. Mao, P. Koppula, W. Cheng, J. Zhang, Z. Xiao, L. Zhuang, B. Fang, J. Chen, S.B. Qian, B. Gan, mTORC1 couples cyst(e)ine availability with GPX4 protein synthesis and ferroptosis regulation, Nat. Commun. 12 (2021) 1589.
[63] C. Hao, X. Wu, M. Sun, H. Zhang, A. Yuan, L. Xu, C. Xu, H. Kuang, Chiral core-shell upconversion nanoparticle@MOF nanoassemblies for quantification and bioimaging of reactive oxygen species in vivo, J. Am. Chem. Soc. 141 (2019) 19373–19378.
[64] F. Shang, M. Lu, E. Dudek, J. Reddan, A. Taylor, Vitamin C and vitamin E restore the resistance of GSH-depleted lens cells to H2O2, Free Radic. Biol. Med. 34 (2003) 521-30.
[65] Y.J. He, X.Y. Liu, L. Xing, X. Wan, X. Chang, H.L. Jiang, Fenton reaction-independent ferroptosis therapy via glutathione and iron redox couple sequentially triggered lipid peroxide generator, Biomaterials 241 (2020) 119911.
[66] Y. Xie, W. Hou, X. Song, Y. Yu, J. Huang, X. Sun, R. Kang, D. Tang, Ferroptosis: process and function, Cell Death Differ. 23 (2016) 369-79.
[67] K.C. Lewandowski, N. Stojanovic, M. Press, S. Tuck, A. Lewinski, M. Karbownik-Lewińska, Raised concentrations of lipid peroxidation products (LPO) in pregnant women with impaired glucose tolerance, Ann. Agric. Environ. Med. 21 (2014) 429-34.
[68] N.A. Fonseca, A.C. Gregorio, V.M. Mendes, R. Lopes, T. Abreu, N. Gonçalves, B. Manadas, M. Lacerda, P. Figueiredo, M. Pereira, M. Gaspar, F. Colelli, D. Pesce, G. Signorino, L. Focareta, A. Fucci, F. Cardile, C. Pisano, T. Cruz, L. Almeida, V. Moura, S. Simões, J.N. Moreira, GMP-grade nanoparticle targeted to nucleolin downregulates tumor molecular signature, blocking growth and invasion, at low systemic exposure, Nano Today 37 (2021) 101095.
[69] Y. Ding, Y. Xu, W. Yang, P. Niu, X. Li, Y. Chen, Z. Li, Y. Liu, Y. An, Y. Liu, W. Shen, L. Shi, Investigating the EPR effect of nanomedicines in human renal tumors via ex vivo perfusion strategy, Nano Today 35 (2020) 100970.
[70] Y. Xu, Y. Guo, C. Zhang, M. Zhan, L. Jia, S. Song, C. Jiang, M. Shen, X. Shi, Differential symptom development and viral RNA loads in 10 nicotiana benthamiana accessions infected with the tobamovirus yellow tailflower mild mottle virus, ACS Nano 16 (2022) 984–989.